ELSEVIER

Contents lists available at ScienceDirect

Geochimica et Cosmochimica Acta

journal homepage: www.elsevier.com/locate/gca





Temperature and co-crystallization effects on Zr isotopes

Heather M. Kirkpatrick ^{a,*,1}, T. Mark Harrison ^a, Mauricio Ibañez-Mejia ^b, François L.H. Tissot ^c, Scott A. MacLennan ^{b,2}, Elizabeth A. Bell ^a

- a Department of Earth, Planetary, and Space Sciences, University of California, Los Angeles, Los Angeles, CA 90095, United States
- ^b Department of Geosciences, University of Arizona, Tucson, AZ 85721, United States
- ^c The Isotoparium, Division of the Geological and Planetary Sciences, California Institute of Technology, Pasadena, CA 91125, United States

ARTICLE INFO

Associate editor: Janne Blichert-Toft

Keywords: Zircon Zr stable isotopes Peninsular ranges batholith SIMS MC-ICPMS

ABSTRACT

We undertook Zr isotope measurements on zircon, titanite, biotite, amphibole, and whole rocks from the La Posta pluton (Peninsular Ranges, southern California) together with trace element analyses and U-Pb age measurements to understand the controls on Zr isotope fractionation in igneous rocks, including temperature, crystallization sequence, and kinetic effects. We find large (>0.6‰) Zr isotope fractionations (expressed as $\delta^{94/90}$ Zr) between titanite and zircon forming at approximately the same temperature. Using equilibrium fractionation factors calculated from ionic and ab initio models, we infer the controls on Zr isotope evolution to include the relative order in which phases appear on the liquidus, with titanite fractionation resulting in isotopically lighter melt and zircon fractionation resulting in isotopically heavier melt. While these models of Zr fractionation can explain $\delta^{94/90}$ Zr variations in zircon of up to ~1.5‰, crystallization order, temperature and presence of corystallizing phases do not explain all aspects of the intracrystalline Zr isotopic distribution in zircons in the La Posta pluton or the large range of Zr isotopic values among zircons (>2‰). Without additional constraints, such as knowledge of co-crystallizing phases and a better understand of the true causes of Zr isotope fractionation, Zr isotopes in zircon remains an ambiguous proxy of magmatic evolution.

1. Introduction

Zirconium was once considered to be isotopically uniform in both terrestrial and extraterrestrial materials (Minster and Ricard, 1981; Minster and Allègre, 1982; Hirata and Yamaguchi, 1999; Hirata, 2001). Subsequently, mass-independent (Schönbächler et al., 2003, 2005; Akram et al., 2013) and mass-dependent isotopic variations have been documented in igneous rocks both at the crystal- (>5‰) (Ibañez-Mejia and Tissot, 2019; Zhang et al., 2019; Guo et al., 2020; Huang et al., 2021; Zhu et al. 2023) and bulk rock-scales (<1‰) (Iizuka et al., 2016; Inglis et al., 2018; Inglis et al., 2019; Feng et al., 2020; Tian et al., 2020; Wu et al., 2020; Yuan et al., 2022) suggesting its use as a tracer of igneous processes (Ibañez-Mejia and Tissot, 2021). While Zr⁴⁺ typically occurs in 6-fold coordination in silicate liquids (Farges et al., 1991; Louvel et al., 2013), it is 8-fold coordinated in zircon (Robinson et al., 1971), the host of most Zr in crustal rocks (Bea et al., 2006). For this reason, mass-dependent equilibrium Zr isotope fractionation is a priori expected

to preferentially partition the light isotope 90 Zr relative to 94 Zr in zircon, driving the melt to isotopically heavier values with increasing differentiation.

A positive correlation reported by Inglis et al. (2018) between whole rock Zr stable isotopes ($\delta^{94/90} Zr$) and SiO2 content among igneous rock standards appeared to yield what would be expected if light Zr isotopes are preferentially fractionated into the crystallizing solid assemblage. Subsequent studies examining Zr isotope variations in natural zircons (Ibañez-Mejia and Tissot, 2019; Tompkins et al., 2020; Guo et al., 2020) and bulk rock samples (Inglis et al., 2019) reported differing apparent zircon-melt fractionation factors. At the bulk-rock scale, Inglis et al. (2019) found a positive correlation between Zr stable isotope values ($\delta^{94/90} Zr_{zircon}$; a few tenths of a‰) and whole rock SiO2 (over ~20 wt% SiO2) (Iceland), suggesting that Zr stable isotopes in whole rocks may track magmatic differentiation. A similar observation was made (Yuan et al., 2022) in rocks from the Shidao alkaline complex (Eastern China). In contrast, at the mineral scale, zircons from the Duluth complex

 $\hbox{\it E-mail address: $hkirkpatrick@fas.harvard.edu (H.M. Kirkpatrick).}$

^{*} Corresponding author.

¹ Now at Department of Earth and Planetary Sciences, Harvard University, Cambridge, MA 02138, United States.

² Now at School of Geosciences, University of the Witwatersrand, Johannesburg 2050, South Africa.

anorthosite (Ibañez-Mejia and Tissot, 2019) revealed >5\% $\delta^{94/90}$ Zr variations that were attributed to a Rayleigh-like chemical removal of isotopically heavy zircon. Subsequently, Tompkins et al. (2020) found no resolvable intra-crystalline variability in a zircon megacryst from the Mud Tank carbonatite from which they inferred that no isotopic fractionation had occurred during zircon crystallization. These three studies imply values for zircon-melt fractionation ($\Delta^{94/90}$ Zr_{zircon-melt}) of +1% (Ibañez-Mejia and Tissot; 2019), 0% (Tompkins et al., 2020) and -0.5% (Inglis et al., 2019). Guo et al. (2020) used intra-crystalline $\delta^{94/90}$ Zr zoning in zircons from the Gangdese batholith to infer variable 94/ $^{90Zr}\alpha_{zircon\text{-}melt}$ (hereafter $\alpha_{zircon\text{-}melt}$) values less than unity, which they hypothesized reflect the strong temperature dependence of the equilibrium isotopic fractionation factor. To address these conflicting results, Chen et al. (2020) and Méheut et al. (2021) investigated possible equilibrium fractionation and nuclear field shift effects by ab-initio calculations, but both predict isotopic variations more than an order of magnitude smaller than those observed in natural samples. Both theoretical studies suggested that kinetic effects in diffusive boundary layers that developed during the crystallization of silicate magmas could provide a viable mechanism for producing%-scale $\delta^{94/90}$ Zr variations recorded in zircon. This inference was recently confirmed experimentally by Tompkins et al. (2023), who confirmed that equilibrium fractionation coefficients between zircon and melt are small as predicted by ab-initio studies, and that kinetic fractionation effects can overwhelm the $\delta^{94/90}\text{Zr}$ variations observed in zircon.

Few phases besides zircon have previously been measured for Zr isotopes resulting in a lack of knowledge surrounding the effects of cocrystallization of zircon with other Zr-hosting phases. While zircon is the principal Zr host in intermediate to felsic rocks, other minerals can accommodate Zr in their structures at relatively high concentrations. Bea et al. (2006) found that titanite and amphiboles from calc-alkaline granitoids contain an average of 853 \pm 559 ppm (n = 74) and 41 \pm 34 ppm Zr (n = 124), respectively. Both minerals can cause middle-rareearth (MREE) depletion in coexisting melt (Simmons and Hedge, 1978; Harper et al., 2004; Colombini et al., 2011) which can then be reflected in co-crystallizing zircon. Thus, we can potentially use these REE signatures to understand the influence of titanite and amphibole crystallization on zircon chemistry. This study investigates these possible effects, by determining isotopic variations not only of zircon but also of other accessory and rock-forming phases in a differentiated plutonic complex. Specifically, we investigate $\delta^{94/90}$ Zr variations in the La Posta igneous suite, an intermediate to felsic suite of granitoids in the eastern Peninsular Ranges of southern California and perform Rayleigh fractionation models to better understand the systematic controls on Zr isotopic variations.

2. The La Posta plutonic suite

The Peninsular Ranges batholith, which extends ~800 km from south of the Transverse Ranges in southern California through portions of Baja California, formed by Cretaceous arc magmatism (Fig. 1). The batholith is broadly calcic in nature (Silver et al., 1979) with compositions varying from gabbroic to granitic (Silver and Chappell, 1988). The Peninsular Ranges batholith has a distinct geochemical and petrologic step (the "I-S line") which strikes N-NW along much of its length and reflects: 1) chemical and isotopic compositional differences (Todd and Shaw, 1985; Silver and Chappell, 1988); 2) the magnetite-ilmenite line (Gastil et al., 1990); and 3) age differences (Krummenacher and Doupont, 1975; Silver et al., 1979; Silver and Chappell, 1988; Walawender et al., 1990; Grove et al., 2003; Ortega-Rivera, 2003; Miggins et al., 2014; Premo et al., 2014; Shaw et al., 2014).

Large, internally-zoned felsic bodies, of which the La Posta suite is the largest, dominate the eastern portion of the batholith (Gastil et al., 1975). These plutons formed by voluminous (75–100 km³/km of batholith strike length/Ma) emplacement of magmas between 98 Ma and 93 Ma (Silver and Chappell, 1988; Kimbrough et al., 2001; Grove et al., 2003). The La Posta pluton was chosen due to the four units being chemically and physically related and the extensive characterization of the pluton along with the variety of Zr-bearing minerals. This pluton is concentrically zoned with whole rock SiO2 values increasing from the hornblende-biotite unit on the outer portion of the pluton to the muscovite-biotite unit in the core (Clinkenbeard and Walawender, 1989). The La Posta suite is characterized by aluminum saturation index $(Al_2O_3/(CaO + Na_2O + K_2O; ASI)$ (Zen, 1986) values of 0.94 to 1.20, initial ${}^{87}\text{Sr}/{}^{86}\text{Sr}$ of 0.70383 to 0.70563, and $\delta^{18}\text{O}$ from 7.2% to 11%, all indicative of a metafelsic source with variable metasediment assimilation (Shaw et al., 2003). The suite is divided into five units ranging from the banded border unit (Clinkenbeard and Walawender, 1989) to a muscovite-biotite granodiorite core with gradational contacts over tens of meters among the inner four units (Walawender et al., 1990). The four units explored here, hornblende-biotite, large biotite, small biotite, and muscovite-biotite, all contain ilmenite. In addition, hornblende and titanite are common in the three outer units (Clinkenbeard and Walawender, 1989) (Figs. 2 and 3).

Zircons from the muscovite-biotite unit have high oxygen isotope ratios (average $\delta^{18}O_{SMOW}=9.18\%$), lower redox state (Trail et al., 2011), and higher P (average P = 690 ppm) concentrations than the outer units, which is consistent with it having assimilated significant pelitic sediment (Bell and Kirkpatrick, 2021). Zircons from the small-and large- biotite units have lower oxygen isotope ratios (average $\delta^{18}O_{SMOW}=8.49\%$) and P concentrations (average P = 367 ppm), indicative of lower sediment assimilation (Bell and Kirkpatrick, 2021). Zircons from the hornblende-biotite unit have high Th/U, U/Yb, and Eu/Eu* indicating deeply forming magmas (Bell and Kirkpatrick, 2021).

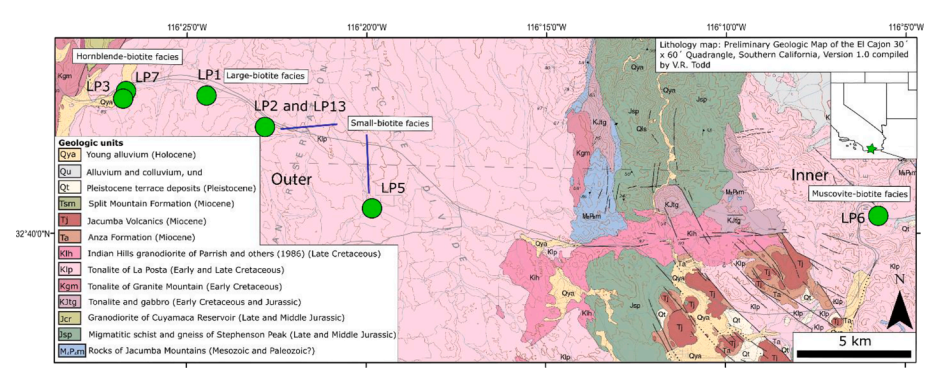


Fig. 1. Geologic map of the La Posta region of the Peninsular Ranges batholith with an inset map showing the location in relation to state lines in the southwestern United States. Geologic map and unit names are from Todd (2004). The green dots show sample locations. From left to right, the units are hornblende-biotite unit (LP3 and LP7), large-biotite unit (LP1), small-biotite unit (LP2 and LP5), and muscovite-biotite unit (LP6). For reference, the light pink unit is the La Posta pluton.

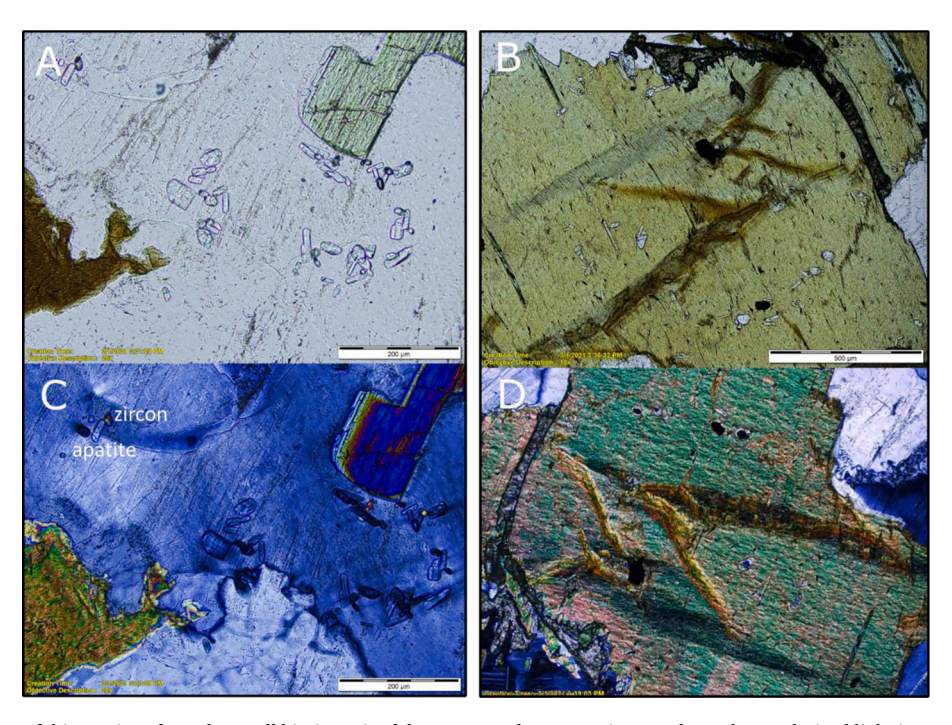


Fig. 2. Petrographic images of thin sections from the small biotite unit of the La Posta pluton. Top images show plane polarized light images and bottom images show cross-polarized light images of samples. Within the black boxes, the images are showing the same area of a thin section (apatite has first order grey birefringence; zircon has 3rd order birefringence). The distribution of zircon is inconsistent with the 'pileup' model, as discussed in Section 5.3.

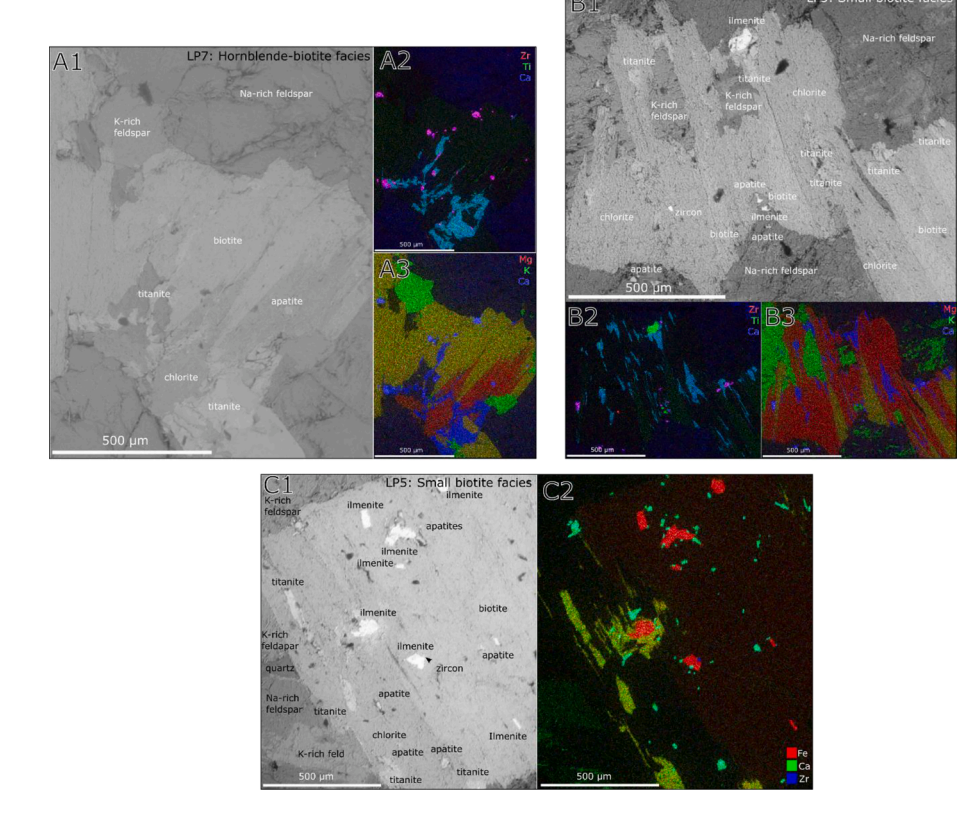


Fig. 3. Images showing the mineralogy of sample LP7 (A) and LP5 (B and C) from the hornblende-biotite and small biotite units of the La Posta pluton, respectively. A1, B1, C1) Backscatter electron images of the studied area with some mineralogy labeled. A2 and 3) show elemental compositions with Zr-Ti-Ca (A2) and Mg-K-Ca (A3) as red-greenblue. Of note, the light blue color and pink in (B) shows titanite and apatite, respectively. P and Zr emit similar x-rays, so these two elements often show up on the others' patterns. The mineral showing red and green in (A3) is biotite. Chlorite is shown in red. Green shows K-rich feldspar, and dark blue shows titanite and apatite. Narich feldspar is black-blue. A1, 2, and 3 show the same field of view. B2) and 3) show Zr-Ti-Ca and Mg-K-Ca, respectively, as red-greenblue. In (B2), light blue shows titanite, green shows ilmenite, pink shows apatite, and red shows zircon. In (B3), blue shows titanite and apatite and red-green shows biotite. C2) shows elemental compositions with Fe-Ca-Zr as red-greenblue. Red shows ilmenite and green shows titanite. Bluish-green shows apatite.

The large- and small-biotite units display Eu/Eu* and Th-U/Yb values which fall between the inner and outmost La Posta units and generally display less clear fractionation trends. From this evidence, Bell and Kirkpatrick (2021) argued that magma mingling was important in the formation of the La Posta suite.

3. Methods

3.1. Sample collection and preparation

La Posta rocks were collected during four field visits between

November 2018 and August 2021 (Table S1; Fig. 1). They were initially processed for zircon separation using a disk mill and powdered with a shatterbox. Once a whole rock split had been obtained, the powder was sieved to $<250~\mu m$ and that fraction panned to acquire the heavy mineral component. A non-magnetic fraction was obtained via a Frantz magnetic separator and a heavy concentrate obtained using heavy liquids. Zircons were then picked from the heavy mineral separate and mounted onto double sided adhesive tape and fashioned into 1" epoxy disks. These discs were polished using SiC, diamond, and/or Al_2O_3 until the mount was optically flat. Using a mortar and pestle, another separate was made; this separate was used for whole rock Zr analyses. Biotite, titanite, and amphibole were picked from one of those two separates. Whole rock sample preparation and XRF measurements were undertaken from splits of the powdered sample at Pomona College following the procedures of Poletti et al. (2016).

From the least differentiated to most differentiated unit: hornblende-biotite zone (LP3 and LP7), large-biotite zone (LP1), small-biotite zone (LP2, LP5, LP13 (no isotope or geochemical information)), and muscovite-biotite zone (LP6). Mineral identification of thick sections was performed through use of the energy-dispersive X-ray analysis attachment on the SEM and analysis of thin sections using a petrographic microscope.

3.2. In situ U-Pb analyses

Using the *ims*1270 at UCLA, we performed U-Pb measurements of zircon following the procedures outlined in Quidelleur et al. (1997), ensuring that inherited zircon cores were not included in our analyses. Measurements of our primary age standard, AS3 and FC1 (1099.1 Ma; Schmitz et al., 2003) were interspersed with every few unknown analyses to monitor instrument drift. All analyses with >95 % radiogenic 206 Pb are included in the compilation and those with both >95% radiogenic 206 Pb and which are within 30% of concordance (Age $_{206/238}$ /Age $_{207/235} \times 100$) are used when comparing ages with zircon isotopic composition. In addition to measurements of AS3 and FC1, we measured Plešovice (Oct, Dec), TanBra (Oct, NovC, Dec), 91500 (Oct, NovA, NovB, NovC), R33 (Oct, NovA, NovB, NovC), and OG1 (Oct, NovA) to assess accuracy.

3.3. In situ trace elements analyses

In-situ trace element analyses of zircon were performed on the CAMECA ims1270 (July 2020, December 2020) and ims1290 (December 2019). Measurements on both instruments followed the procedure outlined in Bell et al. (2016). We use NIST 610 glass as our standard to determine the relative sensitivity factor and compare it against measurements of zircon 91500. We additionally correct for matrix effects on Ti with zircon 91500. Samples with LREE-I (light rare earth index) < 30 and Ti > 30 ppm, both of which indicate likely alteration (Bell et al., 2016; Bell et al., 2019), were removed from further consideration. Most analysis spots for trace elements were targeted to be very near to or overlapping with Zr isotope analytical spots, so trace element, U-Pb, and Zr isotopic analyses can be directly correlated.

For the Ti-in-zircon temperature calculations, we assumed a Si activity ($a_{\rm SiO2}$) of 1 since quartz is present in these rocks (Ferry and Watson, 2007). As rocks with the observed range of Ti-rich phases (i.e., titanite, ilmenite, rutile; Clinkenbeard and Walawender, 1989; this study) typically have $a_{\rm TiO2}$ between ~0.5 and 1.0 (Watson and Harrison, 2005; Reid et al., 2011) we assumed an average value of 0.7. In addition, to understand the impact of Ti activity on temperature-dependent fractionation calculations, we also calculated Ti-in-zircon crystallization temperatures for $a_{\rm TiO2} = 1$. To assess MREE depletion, we calculated a modified Gd/Gd* (Gd/ $\sqrt{\rm (Nd} \times \rm Yb)$) (Colombini et al., 2011).

3.4. Zr isotopic measurements by SIMS

We chose to examine variations in 90 Zr and 94 Zr as both are abundant and neither interfered with at a mass resolving power of ~ 18000 . Our primary standard is Mud Tank zircon, which is homogenous in $\delta^{94/90}$ Zr (Tompkins et al., 2020).

Isotopic measurements were made on seven samples collected from four units. In situ isotopic measurements were undertaken during three sessions using the CAMECA ims1290 with the Hyperion II source (Liu et al., 2018). The first session mainly involved analysis of isotopic reference materials with the latter two sessions primarily focused on analysis of La Posta samples. During the October 2018 and June 2019 session, we used a 5 µm raster, and during the September 2019 session, no raster was used. Analyses were performed using an O³⁻ or O⁻ beam in multicollection mode. During the October 2018 and June 2019 sessions, we measured three masses: ⁹⁰Zr [C detector, Faraday cup (FC)], ⁹⁴Zr [H1 detector, FC], and a dummy background mass [FC1 detector, FCl. During the September 2019 session, we measured two masses: 90Zr [C detector, FC] and 94Zr [FC2 detector, FC]. This change in analysis conditions permitted better background corrections. In the October 2018 and June 2019 sessions a \sim 15 to \sim 18 nA beam was used while the September 2019 session used a ~6 nA beam. This change in beam intensity corresponded with a change from an O⁻ to an O³⁻ beam. These instrument conditions allowed for an \sim 8 μm spot in all sessions. Results are presented in $\delta^{94/90}$ Zr notation defined as:

$$\delta^{94/90} Zr_{sample-standard} = \left(\left[\left(\frac{94Zr}{90Zr} \right)_{sample} / \left(\frac{94Zr}{90Zr} \right)_{standard} \right] - 1 \right) \times 10^3$$
 (1)

where *standard* represents the value of the NIST standard with Mud Tank zircon acting as our lab standard (Tompkins et al., 2020). NIST is the same standard used in multiple previous studies including Ibañez-Mejia and Tissot 2019, Tompkins et al. 2020, and Klaver et al. 2021. $\delta^{94/90}$ Zr for zircons were either calculated by assuming a linear change in the isotopic composition of the standard with analysis number (as a proxy for time; errors calculated using code from Mahon, 1996) of the Mud Tank zircon value to account for instrumental drift, or by taking the mean of all Mud Tank analyses in a session.

Following analysis, samples were examined for inclusions, topography, and cracks in backscatter mode on a Tescan Vega-3 XMU variable-pressure scanning electron microscope (SEM) (Fig. 4). Care was taken to ensure that inherited zircon cores were not analyzed. Imaging using the cathodoluminescence (CL) detector permitted internal structural details of the grains to be revealed.

3.5. Zr isotope analyses by double-spike MC-ICPMS:

For bulk rock analyses, half a gram of sample powder was mixed with 1 g of trace metal grade Li tetraborate flux and 0.3 g of high-purity LiBr non-wetting solution. The mix was fluxed in high purity graphite crucibles at 1100 $^{\circ}\text{C}$ for 10 min, before being quenched in air at room temperature. The resulting glass beads were then fragmented and between 10 and 150 μg of clean fragments (i.e., away from the surface where graphite residues can be found) were dissolved in a volume of 3 M HNO3 + 2 M HF calculated to dissolve the glass.

For mineral separates (biotite, amphibole, and titanite), handpicked grains were rinsed in a mild (1 M) HCl solution for 3 h at 75° C, sonicated, and rinsed twice with MQ-H₂O prior to digestion. Full dissolutions were achieved using five steps: 1) samples were first attacked overnight using 3 ml of 28 M HF + 1 ml 16 M HNO₃ at 130 °C on a hotplate, and then dried to a salt; 2) 4 ml of concentrated aqua regia were added and samples were fluxed overnight at 130 °C until no solids were visible, and then dried to a salt; 3) samples were attacked again using 3 ml of 28 M HF + 1 ml 16 M HNO₃ at 130 °C for 48 h, and then dried to a salt; 4) step 2 using concentrated aqua regia was repeated, and then dried to a salt; 5) 2 ml of 3 M HNO₃ + 0.4 M H₃BO₃ were added to

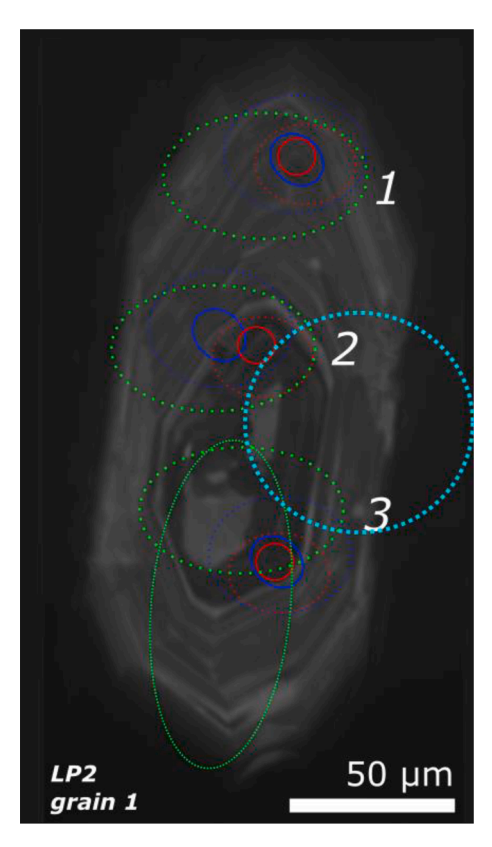


Fig. 4. Cathodoluminescence image of LP2 grain 1 with Zr isotopic analyses, trace element (*ims*1290), trace element (*ims*1270), and U-Pb spots shown in red, blue, light blue, and green, respectively. U-Pb analyses from the November and December 2020 sessions are shown with thicker and thinner dotted lines, respectively. White numbers adjacent to spots show analysis numbers in **Table S4**. This grain contains an inherited core which is Proterozoic in age surrounded by Cretaceous growth.

completely re-digest any remaining fluoride salts. If a solid residue was still visible after fluxing overnight, an additional 2 ml of 3 M HNO $_3+0.4$ M $\rm H_3BO_3$ were added. In all cases this procedure resulted in complete dissolution of the mineral fractions and fluoride salts. Samples were dried one last time to remove fluorine by the preferential production of volatile BF $_3$ gas, and re-digested using 2 ml of 3 M HNO $_3+0.28$ M HF prior to aliquoting for concentration measurement.

After digestion, a small aliquot (~5% of solution) was taken for Zr concentration determinations on an Agilent 7900 inductively coupled plasma mass spectrometer (ICP-MS) at University of Rochester (e.g., Ibañez-Mejia and Tissot, 2019). Once Zr concentrations in the sample solutions were known, samples were spiked with a ⁹¹Zr-⁹⁶Zr isotopic tracer in optimal proportions (i.e., 0.45:0.55 spike-to-sample Zr mass ratio; see Tompkins et al., 2020).

Zirconium purification for all bulk-rock samples and mineral separates followed a four-step ion-exchange procedure where Zr and Hf are first separated from major elements using Eichrom DGA resin. A "matrix clean-up" step was then performed using AG1-X8 resin to ensure complete removal of Fe and other major elements. Subsequently, Zr was separated from Hf using Eichrom Ln-spec resin, and from Mo and Ru, which produce isobaric interferences on several Zr isotopes, using a final clean-up step with AG1-X8 resin. More details on the ion-exchange purification procedure are provided in Ibañez-Mejia and Tissot (2019) and Tompkins et al. (2020).

Zr isotope measurements were performed on the Thermo-Scientific Neptune Plus MC-ICP-MS at the Isotoparium (Caltech) using the same setup and methods as Tompkins et al. (2020) and Klaver et al. (2021). In brief, measurements were made in static mode with faraday detectors monitoring masses 90 to 98. All cups used $10^{11}\ \Omega$ feedback resistors

except for H1 (^{95}Mo) and H4 (^{98}Mo), which used $10^{12}~\Omega$ feedback resistors to improve measurement accuracy for Mo isobaric interference monitoring and corrections. Cup gain calibrations and electronic baselines (60 s, deflecting the ion beam using the Electrostatic Analyser) were performed daily.

Sample solutions containing 70-108 ng/mL Zr in 0.59 M HNO₃ + 0.28 M HF matrix were introduced with an Aridus 3 desolvating nebuliser using a nominal 100 µL/min PFA nebuliser (actual flow rate of 118 $\mu L/min$), which yielded a total Zr ion beam intensity (sample + double spike) of 26-40 V (or about 375 V/ppm of Zr). Each sample was measured two to five times during the session in a non-consecutive fashion. Each unknown measurement was bracketed (linear interpolation) by measurements of a NIST Zr iRM (named RM8299, whose composition is identical to that of the SRM 3169, see Klaver et al., 2021)). Bracketing standards were spiked at the same level as the samples. On-peak-zeros (OPZ) were measured using a 55 s uptake and 20 s on-peak measurement of clean acid solution from the same batch used to dilute the samples, allowing monitoring of memory effects of the sample introduction system. Sample and bracketing standard measurements consisted of 55 s of sample uptake, followed by 50 cycles of 4.192 s integration time each, for a total of ca. 210-250 s of static on-peak sample measurement, consuming ~550 µL of solution. The sample introduction system was rinsed for 360 s between samples using 0.59 M HNO₃ + 0.28 M HF, before repeating the cycle for the next standard/

Data were processed offline employing a minimization approach using all five measured Zr isotopes to solve the double spike equations (see Tompkins et al., 2020). Unlike the conventional DS reduction which only uses 4 isotopes, this approach allows us to check that all ratios are mass-dependently related to one another after DS data reduction. Data are reported as $\delta^{9x}/^{90}\mathrm{Zr}_{NIST}$ (hereafter abbreviated to $\delta^{9x}/^{90}\mathrm{Zr}$), where x can be 1, 2, 4 or 6 depending on the Zr isotope considered in the numerator, relative to a novel Zr reference material (provisionally named RM8299 Zr iRM, interlaboratory calibration ongoing, see Tompkins et al., 2020, for details), and referred to hereafter as NIST. For simplicity, only the $\delta^{94/90}\mathrm{Zr}$ values are shown in figures, but for completeness and to demonstrate the mass dependency of our measurements the $\delta^{91/90}\mathrm{Zr}$, $\delta^{92/90}\mathrm{Zr}$ and $\delta^{96/90}\mathrm{Zr}$ values obtained after DS inversion are also included in Tables 1 and S2. Sample-standard bracketing was performed by linear interpolation using the bracketing standards measured immediately before and after the unknown solution.

For each day of analyses, the dispersion of the standard-bracketed-standard (2SD) for each isotope ratio was calculated using linear interpolation. Uncertainties for individual sample measurements are reported as the 2 SE daily external reproducibility of the standard, rather than the internal precision (i.e., from counting statistics) of each measurement.

Zr-in-titanite temperatures (Hayden and Watson, 2007) were calculated using concentration measurements measured using MC-ICPMS and the same assumptions as those used to calculate Ti-in-zircon temperatures ($a_{\rm SiO2}=1$; $a_{\rm TiO2}=0.7$).

4. Results

4.1. Petrography

Thin section examination of a variety of La Posta suite rocks show that zircon is characteristically found either in clumps (likely formed in late crystallization melt pockets) or as single grains uniformly distributed through the rock (Fig. 2). SEM petrographic observations of thick sections reveal isolated small to large euhedral to subhedral zircon grains included in a variety of host grains (Fig. 3). Crystal textures indicate that titanite forms over a broad range of the crystallization sequence including early (Fig. 3C) and late (Fig. 3B) forming grains. Of note are the euhedral, early forming titanite grains in LP13 (Fig. 5).

Table 1Data from whole rock, amphibole, titanite, and biotite Zr isotope measurements performed via MC-ICPMS.

	phase	n	Zr _{Spk} /Zr _{Tot} *	[Zr] μg/g [‡]	$\delta^{91/90}$ Zr	(±2σ)	Zr stable isotope compositions [§]						Mo interference	
							$\delta^{92/90}$ Zr	(±2σ)	$\delta^{94/90} Zr$	(±2σ)	$\delta^{96/90}$ Zr	$(\pm 2\sigma)$	⁹⁵ Mo/ ⁹⁰ Zr [†]	Mo/Zr ^{††}
Whole r	ocks													
CG1		5	43%	7	-0.026	0.004	-0.052	0.006	-0.101	0.017	-0.150	0.022	5.83E-05	0.012%
LP1-1		5	54%	96	0.003	0.003	0.003	0.011	0.013	0.013	0.015	0.021	9.81E-05	0.017%
LP1-2		5	48%	78	-0.002	0.003	-0.006	0.011	-0.007	0.013	-0.013	0.021	9.99E-05	0.018%
LP2		4	53%	101	-0.013	0.003	-0.032	0.010	-0.050	0.012	-0.079	0.018	1.27E-04	0.021%
LP3		5	49%	84	-0.002	0.003	-0.003	0.011	-0.006	0.013	-0.014	0.021	6.69E-05	0.012%
LP5		5	53%	100	-0.001	0.003	-0.003	0.009	-0.001	0.011	-0.008	0.017	1.54E-04	0.026%
LP6		5	49%	143	-0.006	0.003	-0.017	0.011	-0.022	0.013	-0.036	0.021	1.29E-04	0.023%
LP7		5	49%	89	-0.011	0.003	-0.028	0.009	-0.042	0.011	-0.067	0.017	5.30E-05	0.010%
Mineral	fractions													
LP1-A	Amph.	4	42%	36	0.081	0.003	0.171	0.012	0.316	0.010	0.475	0.018	8.04E-05	0.016%
LP2-T	Titanite	3	45%	656	0.138	0.002	0.271	0.006	0.541	0.010	0.803	0.014	7.36E-05	0.014%
LP3-A	Amph.	3	49%	36	0.074	0.002	0.135	0.006	0.296	0.010	0.431	0.014	1.01E-04	0.019%
LP7-A	Amph.	3	51%	59	0.052	0.002	0.095	0.006	0.208	0.010	0.303	0.014	5.57E-05	0.010%
LP7-T	Titanite	3	47%	320	0.132	0.002	0.258	0.006	0.521	0.010	0.770	0.014	4.26E-05	0.008%
LP7-B	Biotite	3	46%	57	-0.012	0.002	-0.028	0.006	-0.046	0.010	-0.072	0.014	5.15E-05	0.010%

n: number of replicates measured.

^{††} Percent Mo/Zr (atomic).

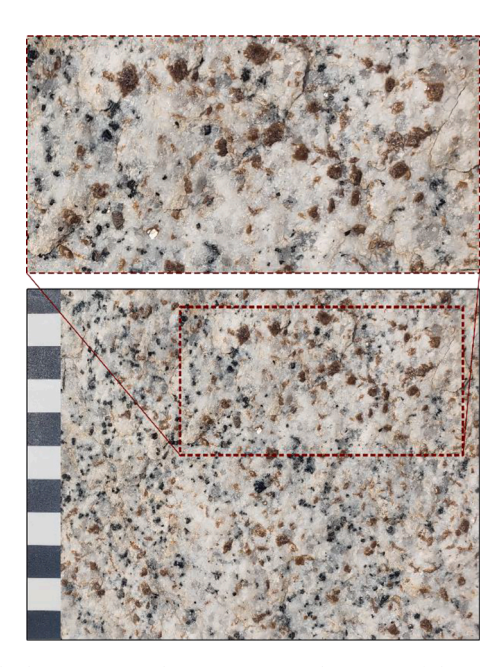


Fig. 5. The bottom image shows a titanite-rich portion of the LP13 outcrop, close to the LP2 sampling location. The burgundy dashed box in the lower image shows the location of the upper image. The vertical measurement of each square on the left side of the lower image corresponds to 1 cm.

4.2. Zircon U-Pb ages

Over five sessions (October 2020, November 2020A, November 2020B, November 2020C, December 2020), we performed 218 U-Pb analyses on La Posta zircons with 145 analyses having % radiogenic ^{206}Pb greater than 95%, and 69 analyses of those analyses being within 30% of concordance (Table S3). Of those 145 spots, 89 spots were matched with a $\delta^{94/90}\text{Zr}$ analysis. In total, 81 spots have trace element and $\delta^{94/90}\text{Zr}$ spots collocated with the U-Pb age (Fig. 6) with 47 of those

analyses being within 30% of concordance (Table S4).

Most U-Pb ages are Late (n = 33 with Zr isotopes, 11 without Zr isotopes) or Early Cretaceous (n = 12 with Zr isotopes, 6 without Zr isotopes) (Table S3, Table S4, Table S5; Fig. 6). However, three ages are Late Jurassic (n = 1 with Zr isotopes, n = 2 without Zr isotopes) and one each are Late Triassic (no Zr isotopes), Late Devonian (no Zr isotopes), Early Devonian (no Zr isotopes), and Proterozoic (with Zr isotope spot) (Table S3, Table S4, Table S5). Among the paired (U-Pb + $\delta^{94/90}$ Zr) analyses, U-Pb ages range between 74 Ma and 148 Ma except for the single Proterozoic age from LP2@3 (LP2 grain 1) where the Zr analysis spot may be impacted by an inherited core as indicated by textural evidence (Fig. 4).

While there is a suggestion that the Zr isotopic composition of zircon becomes lighter with age, the data are highly variable (Fig. 6). The Late Jurassic (PR3_LP3@4: 0.24 \pm 0.11% (1 σ) and oldest Early Cretaceous (PR3_LP3@11: 0.41 \pm 0.13% (1 σ)) analyses are comparatively heavier than the three analyses with ~ 120 Ma ages ($\sim -0.4\%$) (Table S3). However, there is a weak correlation between $\delta^{94/90} Zr_{zircon}$ and age for spots with U-Pb ages between ~74 Ma and 108 Ma. To understand whether there is a relationship between age and isotopic composition at the rock unit scale, we compare paired analyses from the hornblendebiotite unit (samples LP3 and LP7) as well as those from LP3 and LP7 individually. The two isotopically heavy LP3 spots discussed earlier result in a spuriously strong correlation (compared to other Zr isotope and trace element relationships) between age and isotopic composition $(R^2 = 0.48, n = 7)$. LP7, however, shows no correlation between age and isotopic composition ($R^2 = 0.06$, n = 19). Similarly, the small-biotite unit (LP2 and LP5) have no correlation when either analyzed together $(R^2 = 0.03, n = 10)$ or with LP2 alone $(R^2 = <0.01, n = 8)$.

4.3. Trace elements in the La Posta Pluton

Following screening for alteration, 182 trace element measurements of La Posta zircons remained in consideration (Table S6) with 132 of them matching a U-Pb dating spot (Table S3; Table S4). We observe large (>1‰) variations of $\delta^{94/90} \rm Zr$ among zircons within a single rock but little correlation with paired trace elements at the intergrain level

^{*} Fraction of Zr (by mass) from double spike in the spike-sample mixture, calculated by isotope dilution.

 $^{^{\}ddagger}$ Zr concentrations (in $\mu g/g$) determined using isotope dilution.

[§] Reported values are means of all measured replicates for each fraction, expressed as permil deviations relative to the NIST standard according to: $\delta^{9X/90}Zr = ([^{9X/90}Zr]_{Sample}/[^{9X/90}Zr]_{NIST} - 1) * 10^3$. Uncertainites reported for each sample are 2SE, calculated using the daily external reproducibility of the NIST standard (2SD) divided by the square root of the number of replicates measured (i.e., 2SE = $2SD_{External}/\sqrt{n}$).

[†] Ratio of measured ion beam intensities.

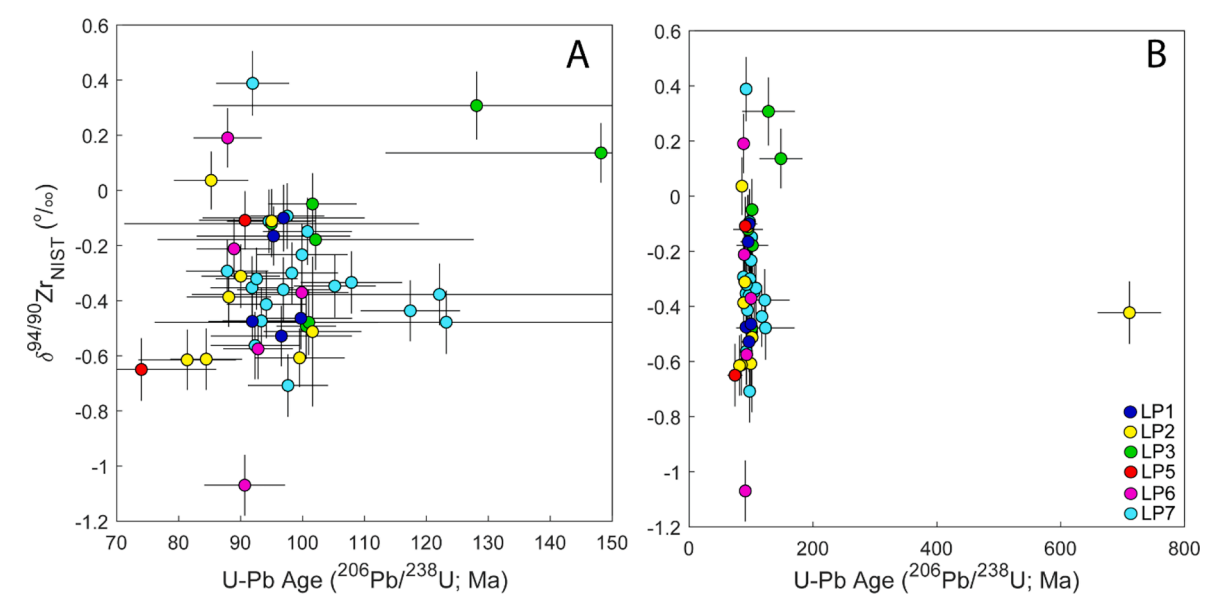


Fig. 6. U-Pb ages vs. Zr stable isotope values of zircons from the La Posta pluton with different colors indicating different samples. All analyses contain >95% ²⁰⁶Pb* and are within 30% of concordance.

(the highest R^2 values are between $\delta^{94/90} Zr$ and Th/U ($R^2=0.05$), Eu_N ($R^2=0.05$), and Sm ($R^2=0.05$)). Hf, generally a strong indicator of magmatic differentiation, shows an even weaker correlation ($R^2=0.05$).

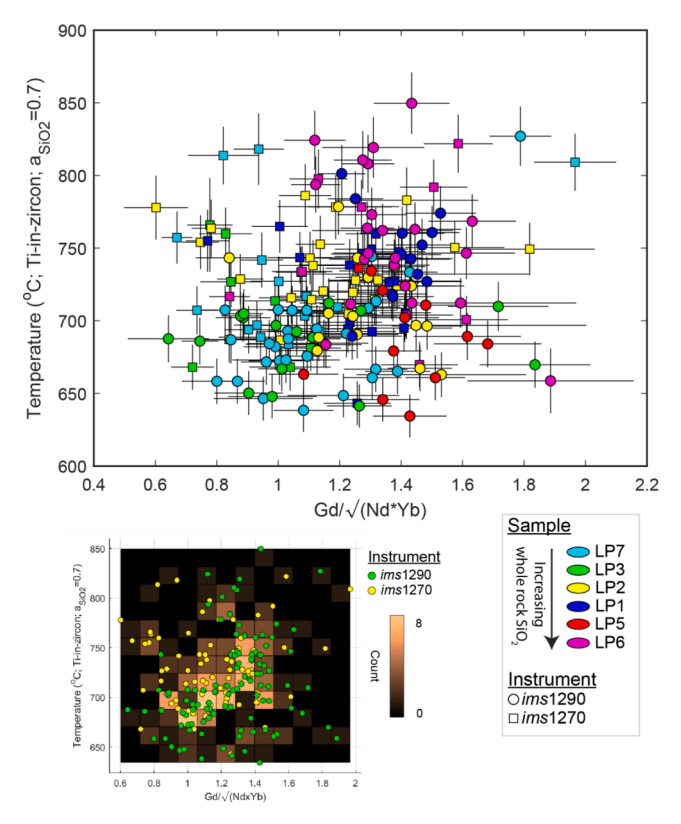


Fig. 7. Gd/Gd^* vs. Ti-in-zircon temperature for all zircons analyzed. Different units within the zoned La Posta pluton are shown in different colors. Generally, less silicic rocks have both lower Gd/Gd^* and lower Ti-in-zircon temperatures showing indicating a higher degree of titanite fractionation prior to zircon crystallization. The heatmap shows an increase in Ti-in-zircon temperature with increasing Gd/Gd^* . Titanite depletes MREE in glasses (Colombini et al., 2011), and Gd/Gd^* is used to represent that depletion here. Square boxes represent analyses made using the ims1270 and circle boxes show analyses made using the ims1290.

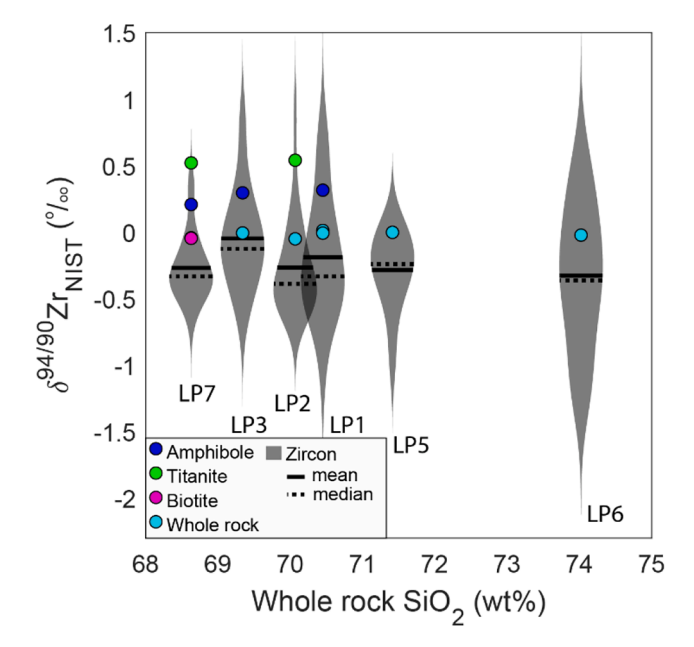
0.01). Although we observe significant intra-zircon $\delta^{94/90}$ Zr variations, these variations do not obviously correlate with CL zoning either. At the intragrain level, R² values between $\delta^{94/90}$ Zr and Th/U, Yb_N/Gd_N, and Mg are only 0.16, 0.10, and 0.07, respectively. The correlation between $\delta^{94/90}$ Zr and Hf is even weaker (R² = 0.03). Using the modified Gd anomaly (Colombini et al., 2011), we observe MREE depletions in zircons from the less differentiated parts of the La Posta suite indicating the presence of one or more additional phase(s) sequestering MREE (Fig. 7). Ti-in-zircon temperatures (assuming $a_{\rm TiO2} = 0.7$), range from 634 to 849 °C. Average Ti-in-zircon temperatures are 734 ± 33 °C, 726 ± 32 °C, 693 ± 31 °C, 688 ± 34 °C, 754 ± 49 °C, and 704 ± 44 °C for zircons from LP1, LP2, LP3, LP5, LP6, and LP7, respectively. These temperatures are plotted in Fig. 7.

LP2 titanite crystallization temperatures are 732 °C and 769 °C for P =0.2 GPa and 0.5, respectively. For sample LP7, temperatures are 694 and 729 °C for P =0.2 GPa and 0.5 GPa, respectively. Changing the α_{TiO2} to 1 result is temperatures $\sim\!20$ °C higher at the same pressure, a_{SiO2} , and Zr concentration.

4.4. In situ standards

Multiple traditional geochemical standards (including AS3, FC-1, Mud Tank, Fishtank, Temora, 91500) were measured with several found to exhibit $\delta^{94/90}$ Zr homogeneity and be within uncertainty of measurements performed using double-spike (DS) MC-ICPMS (Table S7). Two exceptions to this case are AS3 and FC-1 (both from the Duluth anorthosite in Minnesota) which both showed large, multi-‰ variations as previously reported (Ibañez-Mejia and Tissot, 2019; Zhang et al, 2019).

We note that uncertainties of in-situ Zr isotope SIMS measurements are about an order of magnitude larger than those from measurements by bulk dissolution. Currently, studies generally refer to one of three standards, IPGP-Zr (Inglis et al. 2018, Inglis et al. 2019, Zhang et al. 2019, Tian et al. 2020, Guo et al. 2020), NIST (Ibañez-Mejia and Tissot, 2019, Tompkins et al. 2020, Klaver et al. 2021, this study) and SRM 3169 (Feng et al. 2020) with the IPGG-Zr and SRM 3169 standards having a $\delta^{94/90} \text{Zr}_{NIST}$ of $+0.055~\pm~0.002\%$ and $+0.000~\pm~0.007\%$ (Klaver et al. 2021), respectively.



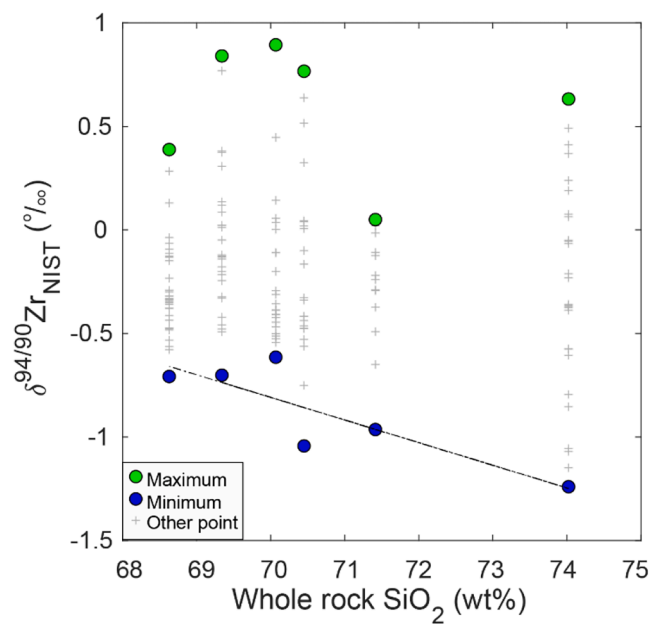


Fig. 8. Top figure shows all Zr isotope analyses in this study: zircons (violin diagram), whole rock (cyan), amphibole (blue), titanite/sphene (green), and biotite (pink). Error bars for whole rock, titanite, biotite, and amphibole analyses, which were conducted by DS-MC-ICPMS, are smaller than the plotted symbols. Black and dotted horizontal lines on the violin plots are mean and median Zr isotopic composition, respectively, of each rock. Note: the biotite and whole rock Zr isotopic composition are approximately the same in sample LP7. The bottom figure shows all Zr isotope analyses of zircon in this study vs. whole rock SiO₂: the zircon with the heaviest Zr isotopic composition (green circle), zircon with the lightest Zr isotopic composition (blue circle), and all zircons measured for each rock (grey cross). Best fit line of each rocks' minimum isotopic composition vs. whole rock SiO₂ shown with a dot-dash line.

4.5. Zr isotopic compositions

Seven La Posta granitoid whole rock Zr isotope analyses range in $\delta^{94/}$ 90 Zr from $-0.050\pm0.012\%$ (LP2) to $+0.013\pm0.013\%$ (LP1-1) (Fig. 8; Tables 1 and S2). Sample CG1 from the cumulate Cuyamaca gabbro, which is largely exposed to the west of the I-S line, yields $\delta^{94/90}$ Zr of $-0.101\pm0.017\%$ (Tables 1 and S2).

We report 153 measurements of Zr isotopes in zircons measured by

SIMS from the La Posta suite (Table S5). As noted earlier, a change in analysis protocol conditions was implemented for the September 2019 session yielding an improved background correction. All La Posta zircon isotopic measurements are from that September 2019 session (Table S5), but we report standards from all three sessions to demonstrate reproducibility (Table S7). Zr isotopic compositions of measurements taken on mount PR3 were calculated by taking into consideration instrumental drift while all other analyses were calculated by averaging our in-situ standard (Table S7-S5).

Apart from LP3, all rocks have mean $8^{94/90} Zr_{zircon}$ between \sim -0.2 and \sim -0.3% (Fig. 8), and the range in $8^{94/90} Zr_{zircon}$ for each rock varies between \sim 1.0 and \sim 1.9% (Fig. 8). While both LP3 and LP7 are from the hornblende-biotite unit and have approximately the same minimum value, LP7 has a smaller range of values than LP3 (LP3: \sim 1.5%; LP7: \sim 1.1%). In addition, the two samples from the small-biotite unit, LP2 and LP5, have ranges of \sim 1.5% and \sim 1.0%, respectively. While we see essentially no correlation between mean zircon (R² = 0.17), maximum zircon (R² = 0.05), or whole rock Zr isotopic compositions (R² = 0.05) for each rock and the associated whole rock SiO₂, we observe a stronger correlation between minimum $8^{94/90} Zr_{zircon}$ and whole rock SiO₂ (R² = 0.73) (Fig. 8). As shown in Fig. 8A, Zr isotopes in zircon generally show an approximate normal distribution within each rock with the median for each rock usually slightly isotopically lighter than the mean.

Isotopic profiles of La Posta grains do not all show similar patterns, even when we only consider grain profiles of zircons from the same rock (Fig. 9). For example, LP2 grain 1, LP3 grain 12, and LP7 grain 7 have profiles which show no isotopic change among the different growth zones. Other grains, including LP3 grain 6, LP3 grain 9, and LP5 grain 5 have slightly heavier isotopic compositions on the outer portion of their respective grains. LP6 grain 2, which appears to have a metamorphic texture, has values mostly between \sim -0.4% and \sim 0.5% yet there is not a distinguishable relationship between location and isotopic composition, even when considering analyses taken on either metamorphic or igneous textured locations. LP6 grain 7 has three spots in the core and inner-mantle with almost uniform isotopic compositions yet the core spot has the lowest Ti-in-zircon temperature. The outer-mantle of this grain has a spot which is \sim 1% higher than the core. LP6 grain 2 has a slightly heavier inner mantle than core and a lighter outer mantle than inner mantle. Even among grains from the same rock, there are not commonalities between isotopic composition and spatial distribution within grains. Information on grain numbers can be found in Table S4.

Results from MC-ICPMS measurements show the $\delta^{94/90}$ Zr of biotite is indistinguishable from the whole rock average of LP7 (average $\Delta^{94/}$ $^{90}\mathrm{Zr_{bio-wr}} = -0.004 \pm 0.014$ ‰, $n_{biotite\ replicates} = 3$; $n_{whole\ rock\ replicates} =$ 5) while titanite and amphibole preferentially incorporate heavier isotopes into their structures (Table S2; Fig. 8). Samples LP1, LP3, and LP7 have average $\Delta^{94/90} Zr_{hbl-wr}$ of 0.313 \pm 0.039, 0.302 \pm 0.008, and 0.250 \pm 0.007‰, respectively (Table S2; Fig. 8). All three values are remarkably similar. The magnitude of Zr isotope fractionation between titanite and whole rock is larger, with average $\Delta^{94/90} Zr_{tit-wr}$ of 0.592 \pm 0.007 and 0.563 \pm 0.007‰, observed in LP2 and LP7, respectively (Table S2; Fig. 8). Concentrations of Zr in amphibole are relatively low (36-59 ppm from three samples; Table S2) thus fractionation of this phase is less likely to strongly influence zircon Zr isotopic compositions given the typical size and modal abundance of amphibole observed in our samples (between <1% to 8.6 %; usually a few hundred μm). In contrast, titanite contains higher Zr concentrations (LP2, 656 ppm; LP7, 320 ppm) and is relatively abundant in La Posta granitoids (up to 10% locally; see LP13 outcrop image in Fig. 5) (Table S2; Fig. 8). Of course, unseen amphibole and titanite cumulates, which are present in the Peninsular Ranges Batholith (Kimbrough et al. 2015), could have influenced the Zr isotopic budget in a fashion for which we have limited constraints.

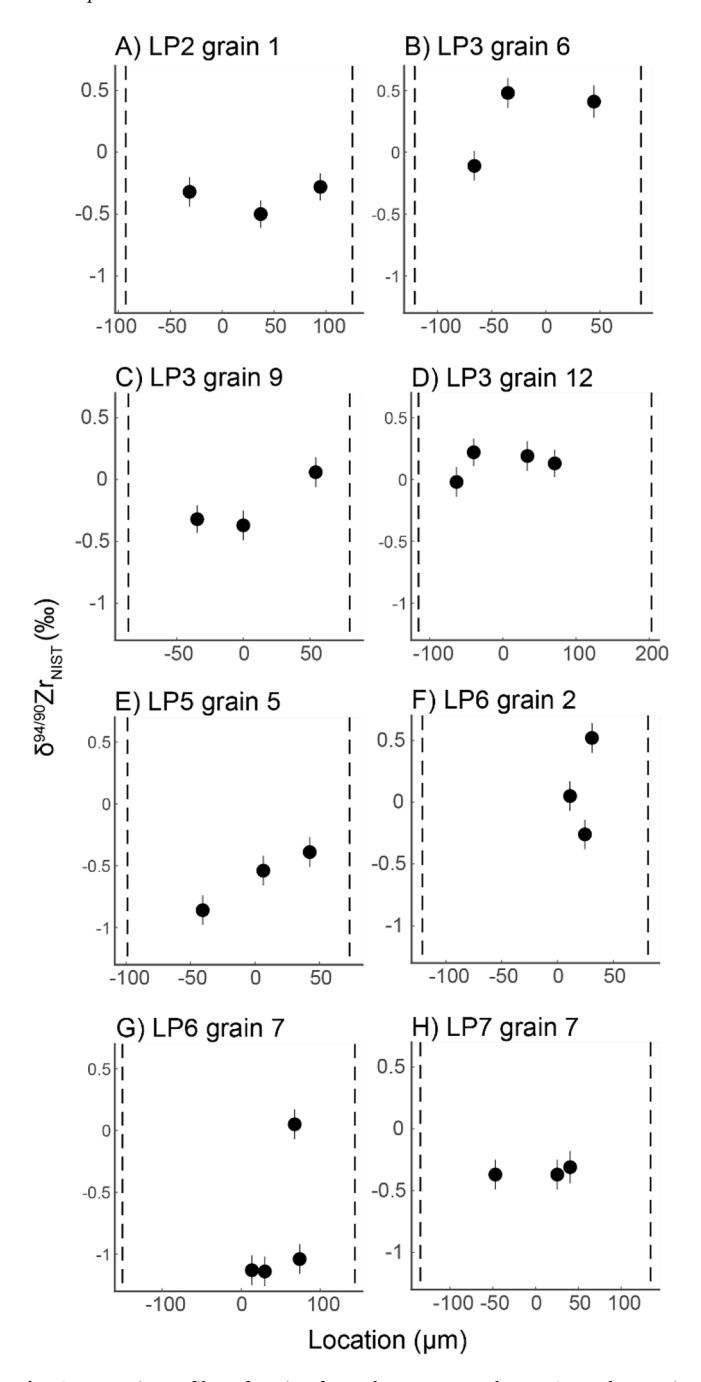


Fig. 9. Isotopic profiles of grains from the La Posta pluton. 0 on the x-axis corresponds to the core of the grain, and the dotted black lines show the edges of grains. Cathodoluminescence images of these grains can be found in the Supplementary Material. Error bars are showing 1 s.d. The width of an analytical spot is less than the horizontal length of a spot.

5. Discussion

5.1. Observations in the La Posta pluton

5.1.1. Applications to understanding magmatic evolution No systematic change of $\delta^{94/90}Zr_{zircon}$, as referenced to the NIST standard, with SiO2 content (over 5 wt% SiO2) is observed in the La Posta granitoids, in contrast to earlier observations from the Hekla magmatic suite (Inglis et al., 2019; over 20 wt% SiO₂ where the majority of change is over <4 wt% SiO₂) and Shidao alkaline complex (Yuan et al., 2022; over 30 wt% SiO2) (Fig. S3). This leaves us to question whether magmatic differentiation is the main control on Zr stable

isotopes.

Among the La Posta samples, we see a variety of Zr isotope grain profile shapes. In LP6 grain 7, LP3 grain 6, or LP3 grain 9, among others, the isotopically heaviest point on this grain is not, as expected if we assume equilibrium Rayleigh fractionation in a closed system, close to the rim of the grain (Fig. 9). Assuming equilibrium fractionation, we would expect to see relatively uniform $\delta^{94/90}$ Zr values until the outermost portion of grains. Many La Posta grains with nearly uniform $\delta^{94/}$ $^{90}\mathrm{Zr}$ values or those with slight increases towards to edge of the grain could thus be explained by equilibrium fractionation. However, grains which are not homogenous indicate that something else is controlling Zr isotope fractionation in this system. Beyond the grain scale, we see >1% variations between different zircon grains in the whole rock sample. These variations at both the inter- and intragrain scale indicate that this system is more complex than the canonical view.

5.1.2. Impact of co-crystallizing phases

Trace elements in zircon can inform us about various processes during zircon crystallization. HREE:MREE in zircon will increase with temperature due to crystal lattice elasticity (lattice strain model: Blundy and Wood, 1994; Blundy and Wood, 2003), and MREE can be depleted by the presence of other phases like titanite, hornblende, or garnet which either crystallized before or concurrently with zircon (Simmons and Hedge, 1978; Whitehouse and Platt, 2003; Harper et al., 2004; Davidson et al., 2007; Colombini et al., 2011). One potential cause of these unexpected Zr isotope values in zircon may be co-crystallizing phases that sequester Zr - such as titanite. For example, Colombini et al. (2011) examined REE patterns for glasses, whole rocks, and titanite from the Highland Range volcanic sequence of southern Nevada. They found that titanite in evolved melts can have $K_{d}>1,\!000$ for the MREE, which is generally higher than partition coefficients in coexisting zircon. In addition, they found a rimward depletion in MREE in titanite indicating a depletion of MREE in the melt during crystallization and apparent partition coefficients for Zr into titanite between 7 and 11.

We observe MREE depletion in low-temperature, later crystallizing zircon, which we argue is a result of the impact of these co-crystallizing phases (Fig. 7). Specifically, the outer three units of the pluton contain significant hornblende and titanite (Walawender and Clinkenbeard 1989). Given the much higher Zr concentration and higher $\delta^{94/90}$ Zr values exhibited by titanite compared to amphibole, we focus mostly on

In addition to rare earth zircon chemistry, petrography and thermobarometry can inform us about the potential impacts of titanite formation on Zr isotopes in zircon. Petrography indicates that titanite formation occurred throughout the crystallization process (Figs. 2, 3), appearing early in the crystallization sequence (see euhedral titanite, Fig. 5), and continuing until the latest stages of magmatic differentiation (see anhedral titanite, Fig. 3). While the late forming titanite likely formed after zircon and would not impact the isotopic composition of the zircon, the early formed titanite may have influenced the melt that zircons eventually formed from. Indeed, for both titanite-bearing samples (LP2 and LP7), Zr in titanite is: (1) isotopically heavier than their respective bulk rock values by very similar magnitudes; and (2) isotopically heavier than most of the zircons in their respective rocks.

For these two samples, we calculated fractionation factors between individual zircon compositions and titanite. To do so, we first calculate the Zr-in-titanite temperature of our two samples. To calculate Zr-intitanite temperatures (Hayden et al., 2008), we estimated an Ti activity (a_{TiO2}) of 0.7 and a Si activity (a_{SiO2}) of 1 due to the presence of titanite and quartz, respectively, and pressure estimates of $0.2\,\mathrm{GPa}$ to $0.5\,\mathrm{GPa}$ GPa, which come from published Al-in-hornblende measurements (Hammarstrom and Zen, 1986; Clinkenbeard and Walawender, 1989) (Table S2). As described earlier, we also calculated Ti-in-zircon temperatures for all grains for which we have trace element data. We then calculate the fractionation factor between titanite and a zircon with a similar crystallization temperature in the same rock. The difference

between the Zr isotopic composition of the zircon and the isotopic composition of the titanite, which crystallized at approximately the same temperature, were $\Delta^{94/90} Zr_{titanite\cdot zrc} > 0.6\%$ (LP2: $0.95 \pm 0.11\%$; LP7: $0.67 \pm 0.12\%$; assuming $a_{TiO2} = 0.7$ and P = 0.5 GPa).

5.2. Modeling fractionation factors and Rayleigh fractionation

5.2.1. Modeling melt evolution

To model the variable inter- and intra-crystalline Zr isotopic composition during crystallization, we assumed Rayleigh distillation in a spherical melt reservoir of a radius containing the total Zr mass in the zircon, with the crystal forming at its center. In our model, isotopic fractionation and zircon growth occur in: (1) isothermal steps and (2) at a constant change in temperature (over $100\,^{\circ}\text{C}$ such that $1\,^{\circ}\text{C}$ reflects a 0.01 change in f), both in a closed system resulting in the partitioning of ^{94}Zr and ^{90}Zr between the solid and melt Zr reservoirs (Fig. 10B, 10D, 11A and E; Fig. S1A and E).

We use the Raleigh distillation model to calculate isotopic composition at each point f,

$$\delta = ((\delta_o + 1000) \times f^{\alpha - 1}) - 1000, \tag{2}$$

where δ is the calculated $^{94}\text{Zr}/^{90}\text{Zr}$ isotopic ratio, δ_o is the starting melt $^{94}\text{Zr}/^{90}\text{Zr}$ composition, α is the temperature-dependent fractionation factor, and f is the fraction of Zr remaining in the melt sphere. The starting temperature was taken as 1006 K, and to account for changing temperature, a revised fractionation factor is then calculated for each new temperature (Figs. 10, 11, Fig. S1). Profiles, which can be used to

either understand the isotopic distribution in a single grain or the isotopic evolution of a system, calculated using $a_{\rm TiO2}=1$ and $a_{\rm TiO2}=0.7$ have very similar trajectories, with the former resulting in a slightly heavier initial $\delta^{94/90} \rm Zr_{zircon}$ (Fig. S2). Because of the similarity, all other profiles are calculated using $a_{\rm TiO2}=0.7$. In the case where zircon is the only Zr-bearing phase under consideration, we assume that all Zr initially in the melt will be incorporated into the growing zircon. In addition, since we are performing in-situ studies, having an idea of the spatial location vs. modeled composition is important. Thus, we plot the Zr isotopic evolution both as the fraction of Zr remaining and spatially (radius-to-volume effects are discussed below) (Fig. 11A, B, E, and F; Fig. S1A, B, E, and F).

The above model assumes that Zr is rapidly equilibrated within the spherical melt reservoir such that its isotopic composition at the crystal growth surface is continuously refreshed to the average value of the remaining reservoir. This assumption is likely valid in hydrous magmas at temperatures typical of zircon formation in intermediate to felsic systems (Harrison and Watson, 1983; Mungall et al., 1999). We estimate the timescale of homogenization to be $\sim\!600$ years using the equation $t=r^2/D$, where D = 6.4×10^{-13} cm² sec^{-1} and r is the radius of our melt sphere. This diffusivity comes from the HPG8 composition in Mungall et al. 1999 (79.64 wt% SiO2, 11.33 wt% Al2O3, 4.88 wt% Na2O, 4.15 wt% K2O, 0.8 ppm Cs, 2.0 ppm Sr, 3.1 ppm Ba, 2.4 ppm Y, 1.2 ppm Nd, 101.0 ppm Zr, 0.2 ppm Nb, 0.0 ppm Ta, 2.7 ppm Hf, 3.7 wt% H2O). This is well within the timescales of igneous systems and long enough that slow Zr diffusion in melt should not cause disequilibrium effects.

The length scale of the melt sphere is determined by the mass of Zr required to form a tabular zircon (i.e., $M_{zir} = 2 \times (4/3 \pi r^3 [Zr]_{melt})$,

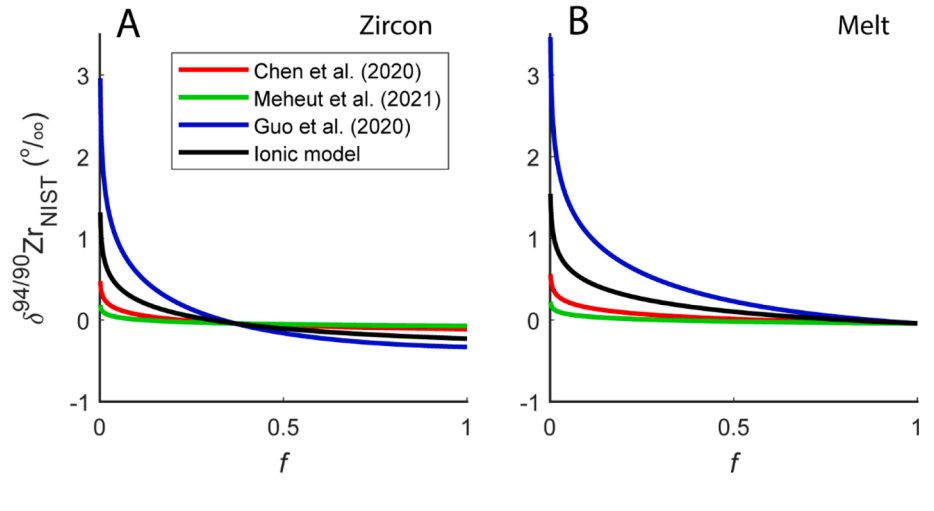
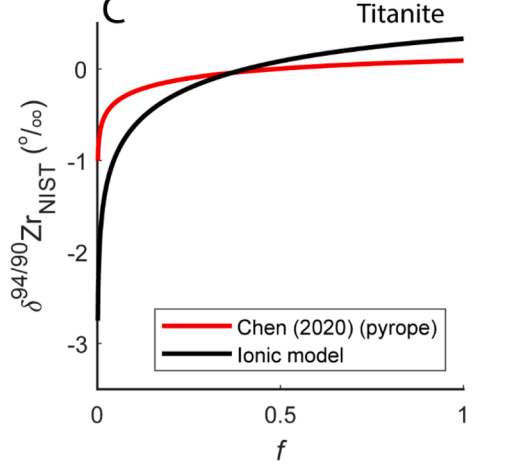
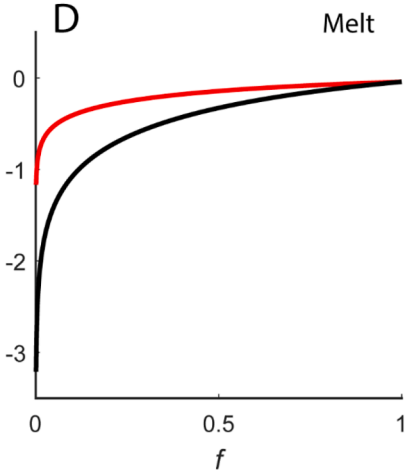
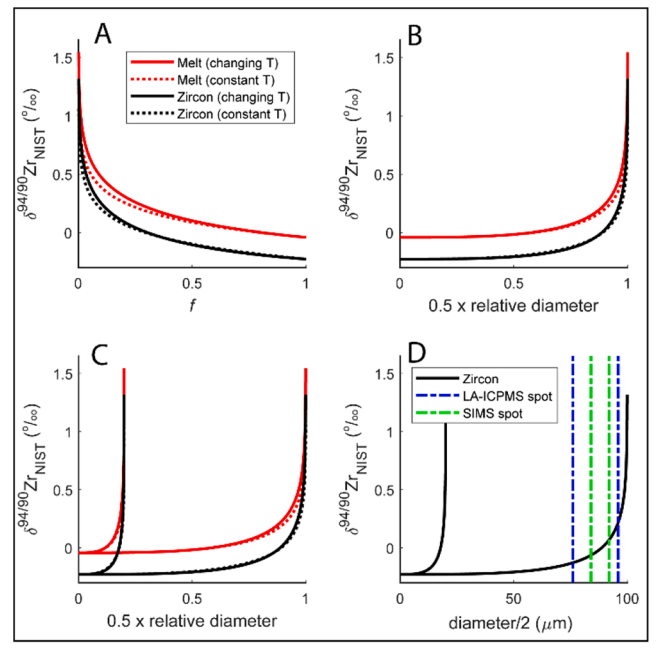


Fig. 10. Modeled evolution curves if only a single phase is crystallizing. A) shows isotope evolution of zircon if zircon crystallizes as a result of Rayleigh fractionation and B) shows the resultant melt evolution. C) shows the Zr isotopic evolution of sphene if it crystallizes alone and D) shows the isotopic evolution of the melt as a result of titanite crystallization. All profiles show a 100 K change ($1006 \rightarrow 906$ K). In the upper two subfigures, zircon is the only phase crystallizing. In the bottom two, titanite is the only phase crystallizing. f is the fraction of Zr remaining in the melt.







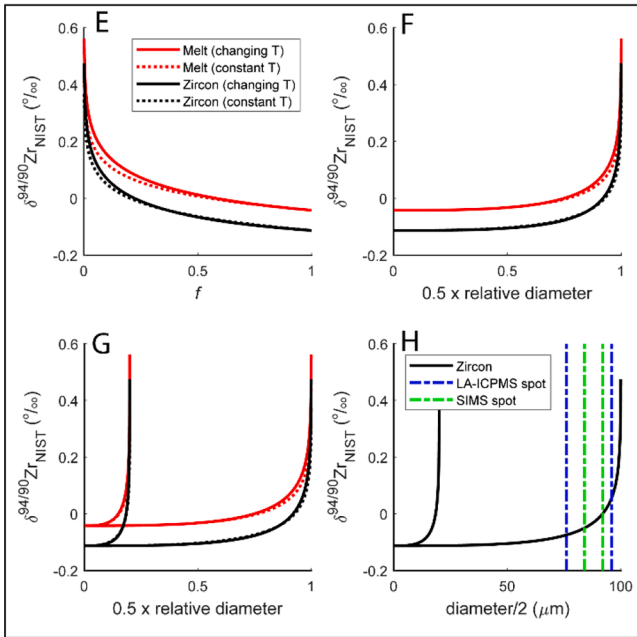


Fig. 11. Red and black lines show the isotopic composition of melt and zircon, respectively and solid and dotted lines show the isotopic trajectory of a system with a constantly changing T and an isothermal system, respectively. A-D show relationships as modeled using the ionic model (Young et al., 2015); E-H show relationships modeled using force constants calculated using values from Chen et al. (2020); A and E) show the relationship between fraction of Zr remaining in a system and modeled Zr isotope composition. B, C, F, G) Modeled zircon isotope profiles showing the impacts of constant vs. changing T on Zr isotope evolution for a tabular zircon that we model as a rectangle. B and F) shows a system where all three zircon axis are the same length (x = y = z) and C and G) shows a system where x = y and z = 5x. D and H) shows a grain where z = 200 µm and z = y = 40 µm along with the approximate size of LA-ICPMS and SIMS beams in blue and green, respectively.

where $M_{\rm zir}$ is the mass of Zr in the zircon, 2 is the ZrSiO₄/Zr weight correction factor, r is the radius of the melt reservoir, and [Zr]_{melt} is the concentration of Zr in the melt. For a grain with an effective spherical radius a of 90 μ m (i.e., the spherical mass equivalent of a tabular zircon) that formed from a melt package where [Zr]_{melt} = 140 ppm, the radius of

the required melt reservoir is ${\sim}1100~\mu m.$ Examples of Rayleigh fractionation curves due to continuous zircon removal from a melt, calculated using the above methods, are shown in Fig. 10A and B, respectively. All modeled zircon fractionation factors, $\alpha_{zircon\text{-}melt}$, are less than 1.

5.2.2. Zircon-melt fractionation factors

Due to discrepancies among reported zircon-melt fractionation factors (Méheut et al., 2021; Chen et al., 2020; Guo et al., 2020), we calculate temperature-dependent fractionation factors using three general models: (1) ab initio calculations, (2) an ionic model, and (3) the regression reported in Guo et al. (2020) between 1000 $\ln\alpha_{zircon-melt}$ and $10^6/T^2$. These fractionation factors are calculated with (1) isothermal steps and (2) at a constant change in temperature (over 100 °C such that 1 °C reflects a 1% total change in remaining Zr).

Two studies report force constants calculated using ab initio methods (Chen et al., 2020; Méheut et al., 2021). Using Ca-catapleiite as a model structure for silicate melts, Chen et al (2020) reported force constant, K_f , for zircon and Ca-catapleiite of 334.7 N/m and 369.2 N/m, respectively. Using vlasovite as their model structure for the melt, Méheut et al. (2021) reported K_f values for zircon and vlasovite of 392.7 N/m and 407.8 N/m, respectively. Using these force constants, we calculate the β factor for both melt and zircon as:

$$1000 ln \beta(^{94} Zr/^{90} Zr) \simeq 2081.6 K_f/T^2$$
 (3)

where K_f is the force constant, β is the reduced partition function ratio, and T is the temperature in Kelvin (Chen et al., 2020; Méheut et al., 2021). We then calculate the zircon-melt fractionation factor for each set of force constants using

$$\ln \alpha_{\text{product - reactant}} = \ln \beta_{\text{product}} - \ln \beta_{\text{reactant}}$$
 (4)

where the product is zircon and the reactant is melt.

Second, we calculate isotope fractionation factors using an ionic model. Ionic force constants, K_f (Young et al., 2015), were determined using

$$K_f = \frac{z_i z_j e^2 (1 - n)}{4\pi \epsilon^o r_o^3} \tag{5}$$

where z_x are the cation and anion valences, e is the charge of an electron (in C), n is 12, e^o is vacuum permittivity (in $C^2N^{-2}m^{-2}$), and r_o is the equilibrium interionic distance (in m). Interatomic distances were obtained from Robinson et al. (1971) and CrystalMaker®, and ionic force constants were calculated for each different interatomic distance in zircon. Since the Zr coordination polyhedron in zircon is a distorted octahedron, four of the bond lengths are 2.268 Å and four are 2.131 Å. The ionic force constants for all bonds are averaged and used to calculate a fractionation factor. We assume 2.10 Å for melt (haplogranite), however the Zr-O bond length is variable depending on the composition of the melt of interest (Louvel et al., 2013). This results in K_f of 1914 N/m and 2186 N/m for zircon and melt, respectively. We then calculate the fractionation factor as:

$$ln\alpha_{A-B} = \frac{1}{24} \left(\frac{h}{k_b T}\right)^2 \left(\frac{1}{m_l} - \frac{1}{m_h}\right) \left[\frac{K_{f,A}}{4\pi^2} - \frac{K_{f,B}}{4\pi^2}\right]$$
 (6)

where h is Planck's constant, k_b is the Boltzmann constant, T is temperature (in K), m_l is the mass of the light isotope (90 Zr), m_h is the mass of the heavy isotope (94 Zr), K_f is the force constant, phase A is zircon, and phase B is the melt (Young et al., 2015).

Third, we used the empirical temperature-dependent isotope fractionation relationship of Guo et al. (2020) (Table S6):

$$1000 \ln \alpha = -0.95x + 0.65 \tag{7}$$

where x is $10^6/T(K)$ and T for that spot is determined from Ti-in-zircon

thermometry (Watson and Harrison, 2005). We do this for illustration and comparison purposes despite questioning the accuracy of the Guo et al. (2020) calibration (which they acknowledge as provisional). Specifically, the slope of the regression appears too large (e.g., yields factor of 2 isotopic fractionation over <100 $^{\circ}$ C intervals and \sim 11‰ at 30 $^{\circ}$ C) to be physically meaningful and the regression predicts non-zero fractionations at infinitely high temperature, which violates the principles of equilibrium stable isotope fractionation. As shown in Fig. 10, fractionation calculated by this method are approximately an order of magnitude higher than those proposed by ab initio calculations and several times higher than those calculated using ionic models. As discussed in Méheut et al. (2021), the isotope profiles in zircon grains reported in the Guo et al. (2020) study may be dominated by kinetic fractionation making this a poor choice for determining equilibrium fractionation factors. Beyond this, the temperature dependence (Eq. (7) is statistically weak with large scatter. This, and the unreasonably large effects this relationship predicts at both low and infinite temperature, leads us to argue against its use in determining temperature-dependent fractionation factors. Lastly, we note that the difference between K_f for our phases, rather than the value of each K_6 is what controls the magnitude of isotope fractionation.

5.2.3. Titanite-melt fractionation factors

Since we do not at present have a provisional temperature-dependent isotope fractionation calibration for titanite as we do for zircon (see 5.2.1.), we estimate the titanite-melt fractionation factors a variety of ways. First, using force constants calculated via density functional theory in Chen et al. (2020) ($K_{f, pyrope} = 433.5 \text{ N/m}$ and $K_{f, melt} = 369.2 \text{ N/m}$) and Eqs. (3) and (4), we calculate the Zr isotope fractionation between melt and a titanite proxy. We use data from the $^{IV}Al^{3+} + ^{1V}Si^{4+} \leftrightarrow Zr^{4+} + Al^{3+}$ substitution in pyrope as a proxy for Zr substitution in titanite, because both Ti in titanite and Zr in the octahedral site in pyrope have similar cation-oxygen lengths and both bonds are in the same coordination (Chen et al., 2020). Ca-Catapleiite, which we use to understand the structure of the melt when looking at zircon-melt fractionation, is again used as a proxy for melt.

Second, we calculated fractionation factors using an ionic model. Ionic force constants are calculated using Eqs. (5) and (6) where phase A is titanite and phase B is the melt. Zr in titanite is in an octahedrally coordinated site, and we used CrystalMaker® to determine the interatomic distances for each bond (1.766 Å, 1.974 Å, 1.984 Å, 1.991 Å, 2.025 Å, and 2.014 Å) (Speer and Gibbs, 1976). Ionic force constants for each bond were calculated, and an average was then used to calculate a fractionation factor. As described previously, we use 2.10 Å for melt Zr-O distance (Louvel et al., 2013). The titanite-melt fractionation factors, $\alpha_{titanite-melt}$, estimated are greater than 1.

An alternate method to assess temperature effects on Zr isotope fractionation into titanite would be to calculate the titanite-melt fractionation factor using the measured titanite and the measured whole rock values (Table S2), and then regress these values with the sample temperature. Temperatures for this calculation could be determined via average Zr-in-titanite crystallization temperatures for each rock (Hayden et al., 2008). This approach, similar to the method of Guo et al. (2020), is however not appropriate where both zircon and titanite are significant reservoirs of Zr due the paucity of documented titanite-rock fractionation factors. This is further complicated by the closeness of these two samples' average Ti-in-zircon and Zr-in-titanite temperatures. This results in a regression with very large error bars that trends positive rather than negative as expected from first principles.

5.2.4. Difference between fractionation factors

As shown in Figs. 10 and S1, the four approaches for determining zircon-melt fractionation factors and the two approaches for titanite-melt fractionation factors yield contrasting results. For example, while the fractionation factors calculated from the two different ab initio studies (Chen et al., 2020; Méheut et al., 2021) produce similar, and

limited fractionations (\sim 0.15‰) in the final stages of zircon growth (after 95% of melt crystallization), the ionic model produces effects several times larger (\sim 0.7‰). The largest effects are produced when using the fractionation factors derived from empirical temperature-dependent isotope fractionation relationship of Guo et al. (2020).

Because the ionic model is based on Pauling's rules whereas ab initio models explore mineral bonds at the quantum level, the two methods typically produce results that are within a factor of 2 or 3 of each other (Young et al., 2015). We use the ionic model as it allows for direct calculation of the titanite fractionation factor without assumptions on the similarity of bonding environments - and force constants - in compositionally different minerals, as was done in the ab-initio estimation through the use of garnet as a proxy for titanite. A drawback is that this method is hindered by the lack of known Zr-O interatomic distances in melt. While we do not have exact values of this parameter, interatomic distances of zircon and titanite are determined to be larger and smaller, respectively, compared to melt in other studies (Robinson et al., 1971; Farges et al., 1991; Louvel et al., 2013; Chen et al., 2020). Therefore, while the force constants will be slightly different depending on what Zr-O bond lengths are used for melt, titanite has $\alpha_{titanite-melt} > 1$ and zircon has an $\alpha_{\text{zircon-melt}} < 1$ allowing for a basic understanding of fractionation (Fig. 10).

In addition, we note that zircon isotopic values for each rock cover a large range of values. When directly comparing the measured isotopic values of zircon and whole rock ($\alpha_{zircon\text{-}melt}=(1000+\delta^{94/90}Zr_{zircon})/(1000+\delta^{94/90}Zr_{whole}$ rock)), most $\alpha_{zircon\text{-}melt}$ are less than 1 showing that while the magnitude of $\alpha_{zircon\text{-}melt}$ are different between those calculated from natural samples and those calculated using our various models, the signs are the same. $\alpha_{titanite\text{-}melt}$, calculated using measured titanite and whole rock samples, are both greater than 1. This is also the same sign as $\alpha_{titanite\text{-}melt}$ calculated using our models.

To proceed, we used the Chen et al. (2020) ab initio values and the ionic model as the most promising approaches; the Chen et al. (2020) study provides force constants for zircon, melt, and a titanite proxy while the ionic model allows us to directly compare titanite and zircon fractionation. We do not show calculation of fractionation between zircon-melt and a titanite proxy-melt using values from Méheut et al. (2021) because they do not publish force constants for titanite. However, Fig. 10 shows Rayleigh fractionation curves of zircon calculated using K_f values from Méheut et al. (2021). Comparisons of Rayleigh fractionation curves and La Posta isotope and trace element are shown in Fig. 13.

5.2.5. Modeling the impact of co-crystallizing phases on zircon isotopic composition

Rocks of the La Posta series crystallized under hydrous conditions, yielding relatively uniform distributions of zircon at the hand sample scale. Thus, we chose to investigate the coupled effects of temperature and simultaneous growth of multiple Zr-bearing phases as a possible source of the observed 1 to 1.9% $\delta^{94/90}$ Zr variations in La Posta zircon. Predicting the isotopic composition of Zr in zircons forming from a silicate magma is complicated by our lack of knowledge of the crystallization and fractionation histories of those zircons, the presence of cocrystalizing Zr-bearing phases (e.g., titanite), and the thermal history of the magma. To untangle these complexities, we calculated crystallization temperatures to gain insights into the possible co-crystallization of zircon (Watson and Harrison, 2005) and titanite (Hayden et al., 2008) and utilize the known diffusion parameters for Zr in hydrous silicate melts (Watson and Harrison, 1983; Mungall et al., 1999) to assess the likelihood of isotopic equilibrium being maintained during some specified thermal evolution. Rather than viewing the problem as simply an exchange between bulk melt and zircon, we now chose a model that places individual zircons in context with the melt volume required to fertilize the growing zircon described earlier.

We therefore undertook a series of calculations to assess the potential impact of titanite on the Zr isotopic composition of La Posta zircons. In

our illustrative examples, we assume: 1) titanite and zircon temporally co-crystallize; 2) Zr is drawn from within a spherical reservoir assuming its diffusivity is high with respect to growth rate of zircon and titanite; 3) the radius of the reservoir sphere is equal to the final mass of zircon and titanite (i.e., $M_{Zr\text{-zircon}} + M_{Zr\text{-titanite}} = 2 \times (4/3 \pi r^3 [Zr]_{melt})$); and 4) the growth of titanite and zircon occurs in steps with a constant lowering of temperature (as in our modelling of melt evolution, with 1 °C steps over 100 °C) resulting in the partitioning of two isotopes between three reservoirs as the melt reservoir decreases in size and material is constantly removed with instantaneous solid-melt fractionation represented by $\alpha.$ We then model the relative fractions of each phase required to realize equal Zr consumption. Taking the highest [Zr] value we observe in titanite (i.e., 656 ppm in LP2) and the typical concentration of Zr in zircon (~480,000 ppm), this translates to a zircon:titanite Zr concentration ratio of ~730. Thus, for the case in which titanite constitute 5% of modal phases, which is within the range of modal abundances found in this unit (Fig. 5), we would expect a zircon abundance of ~70 ppm, which is similar to values from the La Posta pluton. This value can then be used to determine how much titanite would need to be removed to have a specified effect in the zircon. Titanite modal abundances are normally lower than this calculated value. To understand Zr isotopic evolution in these rocks, we modeled three compositions: $P_{zircon} = 50\%$ and $P_{titanite} = 50\%$, $P_{zircon} = 75\%$ and $P_{titanite} = 25\%$ and: $P_{zircon} = 90\%$ and $P_{titanite} = 10\%$, where P_x is equal to the proportion of Zr that partitions into phase 'x' (Fig. 12). We calculate the effective fractionation factor for the melt as $\alpha_{solids-melt} = (P_{titanite} \times$ $\alpha_{titanite-melt, T}$) + ($P_{zircon} \times \alpha_{zircon-melt, T}$) where $\alpha_{solids-melt}$ is the fractionation factor between solids and melt, P_{phase} is the proportion of Zr partioning into either zircon or titanite, and $\alpha_{phase-melt, T}$ is the temperature-dependent fractionation factor between either zircon or titanite and melt. To determine the isotopic composition of instantaneous zircon and titanite at each f, we use the equations

$$\delta_{melt} = \left(\delta_{melt,0} + 1000\right) \times f^{\alpha_{solid-melt}-1} - 1000 \tag{8}$$

and

$$\delta_{phase} = \delta_{melt} + (P_{phase} \times \varepsilon) \tag{9}$$

where $\epsilon=1000~ln\alpha_{phase-melt}$ to the melt composition at that f. Since $\alpha_{zircon-melt}<1$ and $\alpha_{titanite-melt}>1$, the concavity of the $\delta^{94/90}Zr$ vs. f (when looking at the isotopic evolution of a rock) or diameter/2 (when observing the isotopic evolution of a grain) changes from concave to convex depending on the amount of each phase being formed at that specific f (Fig. 12).

To understand the impact of crystallization order on Zr isotopic evolution, we modeled a series of isotopic evolutions (Fig. 14). In every case, the systems contain 50% of Zr held in zircon and 50% in titanite. In scenario 1, titanites crystallizes alone for the first 25 °C (f=1 to f=0.75) followed by 1/3 and 2/3 of the remaining Zr incorporated into titanite and zircon, respectively. In the second scenario, only titanite crystallizes until f=0.50 followed by only zircon until f=0. Fractionation of a single-phase results in a greater range of instantaneous isotopic values for each phase than when there is co-crystallization and co-crystallizing phases with near opposite fractionation factors dampen the fractionation experienced by the melt and crystallizing phases. (Fig. 14). This is relevant when considering either flat profiles extracted from insitu analyses or when looking at the range of isotopic values of zircons at the hand sample scale.

While titanite fractionation cannot account for the entirety of the fractionation seen in the La Posta pluton, it can, and likely has, accounted for at least some of it. In our current model where δ_0 is the whole rock composition, the models do not predict either the measured

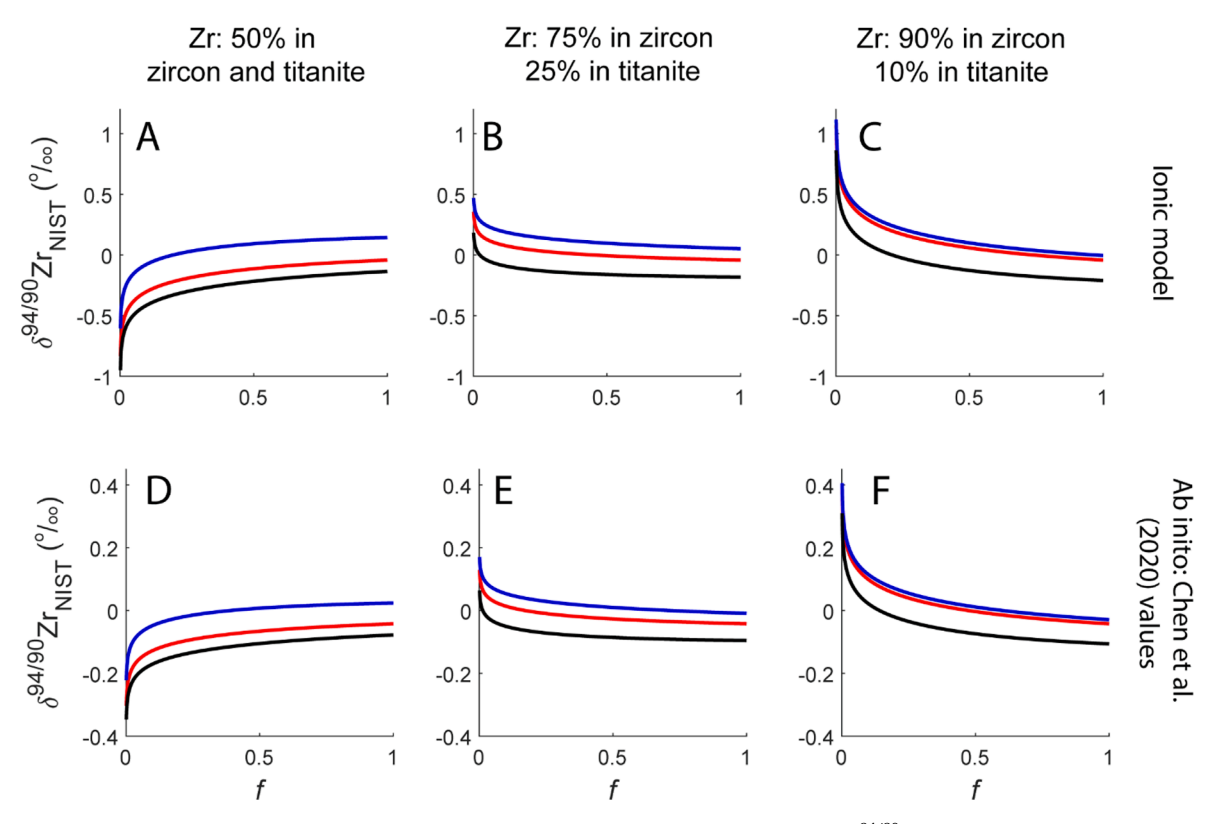


Fig. 12. Influence of co-crystallizing phases on isotope profiles shown through fraction of Zr remaining (f) vs. $\delta^{94/90}$ Zr (‰) for a modeled zircon for a system with a constant change in temperature. Red, blue, and black lines show the isotopic composition of melt, titanite, and zircon, respectively. Figures A-C show fractionation factors calculated using the ionic model. Figures D-F show profiles calculated using fractionation factors calculated using values from Chen et al. (2020). Please note the differences in the y-axis between profiles calculated using the ionic model (A-C) and those calculated using the ab initio method (D-E). In addition, please note that the range of measured values is greater than displayed in this figure.

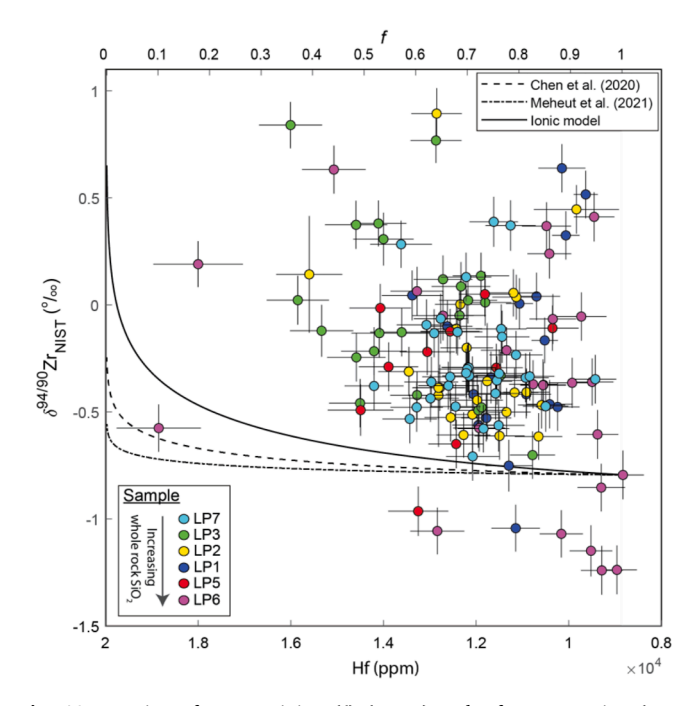


Fig. 13. Fraction of Zr remaining (f) (upper) and Hf concentration (ppm; lower) vs. $\delta^{94/90}$ Zr (‰) for a modeled zircon where $\alpha_{Ti}=0.7$ and there is a constantly changing T. The starting zircon isotopic composition is from the zircon analysis with the lowest Hf concentration. All other points where both Zr isotope and Hf concentration information are available are plotted as well. Dashed, dot-dashed, and continuous lines are show for fractionation lines calculated from information provided by Chen et al. (2020), Méheut et al. (2021), and from the ionic model.

zircon or titanite isotopic values. For example, in a system where 50% of Zr is incorporated into zircon followed by the remaining 50% incorporated into titanite, we never reach the isotopically heavy titanite or the very isotopically light zircons observed, regardless of whether we use the ionic model or models based on ab initio calculations.

Initial melts could have been isotopically heavier than the whole rock Zr isotopic values we measured if isotopically heavy titanite was removed from the system. We observe this could potentially be the case due to the much higher amount of titanite observed in sample LP13 (Fig. 5), which comes from the same outcrop as LP2. However, even with this assumption, our model will still not predict the observed extremely isotopically light La Posta zircons.

5.2.6. Timescales of melt homogenization and potential impacts of a diffusive boundary layer

We can get a first order estimate of the timescale for homogenization using the 1-D approximation $t = r^2/D$, where t is time, r is the radius of the reservoir sphere (\sim 1100 μ m), and D is the Zr diffusivity (D = 6.4 \times 10^{-13} cm² sec⁻¹; Mungall et al. 1999). This suggests that the time it would take for the model zircon grain to form is only about 600 years. However, this assumes that all Zr is removed from the reservoir sphere whereas only that portion above the level of zircon saturation in the melt can be sequestered at any moment. This requires a more complex calculation that involves decreasing zircon solubility with cooling (Watson and Harrison, 1983; Boehnke et al., 2013). Watson (1996) undertook such an analysis, principally for the case of zircon dissolution but as both processes are controlled by the absolute melt solubility, level of over/undersaturation, and Zr diffusivity (rather than being interface controlled), these results provide complementary insights into crystallization timescales as well. For plausible values for the La Posta case (i. e., Zr oversaturation of 20 ppm, cooling rate of 0.01 °C/yr; see Fig. 8 of Watson, 1996), a 90 μ m radius zircon is estimated to form in ~10,000 years. This timescale is both commensurate with known U-Th ages of young magmatic zircons (Reid et al., 1997; Schmitt, 2011) and sufficiently long (as illustrated by the heuristic calculation above) for Zr isotopic homogeneity in a hydrous magma to be continuously achieved by diffusion within the reservoir shell. While this model presupposes no ingress of Zr into the reservoir sphere during zircon crystallization, a seemingly unrealistic assumption at first glance, a stochastic distribution of zircon nuclei spaced roughly at the characteristic Zr diffusion distance would have the effect of approximating a zero Zr flux boundary condition at the shell perimeter (Bindeman and Melnik, 2016). Sample petrography is broadly consistent with this assumption with clumps of zircon formed in melt pockets often appearing together in thin section (Fig. 2).

Méheut et al. (2021) argued that large fractionations can be caused by kinetic imbalances between crystal growth, chemical diffusion in the melt, and the mass dependency of diffusing isotopes. Specifically, a diffusive boundary layer may develop within the melt near the surface of a fast-growing mineral with low partition coefficient for Zr, resulting in higher [Zr] and $\delta^{94/90}$ Zr near the mineral-melt interface (referred to as the pileup effect). Assessing the relevance of a diffusive boundary layer is complicated by the lack of knowledge of the calibration parameter, β , (from equation $D_{94}/D_{90} = (m_{90}/m_{94})^{\beta}$, where D_{x} is the diffusion coefficient and m_x is mass) which describes the magnitude of mass dependent diffusive separation between two isotopes (e.g., 94Zr and 90Zr) and the assumption of anhydrous crystallization conditions. Nevertheless, the proposal of Méheut et al. (2021) appears viable in the case of rapidly crystalizing volcanic and hypabyssal magmas because of the much faster zircon crystallization (and thus higher growth to diffusion ratio) compared to plutonic systems. The relevance of this process to the plutonic rocks under study is, however, unclear as in such hydrous plutonic rocks the diffusivity in the melt is faster than the growth rate of the crystal. Therefore, an enriched diffusive boundary layer should not exist.

Méheut et al. (2021) argues that the profiles observed in Guo et al. (2020), which are from zircons formed in the hydrous Gangdese Batholith, indicate kinetic rather than equilibrium fractionation due in part to the high zircon growth rate to Zr diffusion in melt ratio (R/D). While this is true for anhydrous melts (e.g., R/D is $\sim 3 \times 10^4~{\rm cm}^{-1}$ for a growth rate of $10^{-13}~{\rm cm~sec}^{-1}$ at $740~{\rm ^{\circ}C}$; Mungall et al. 1999), wet melts have a R/D less than 1 (e.g., R/D is 5×10^{-2} for a growth rate $10^{-13}~{\rm cm~sec}^{-1}$ at $740~{\rm ^{\circ}C}$; Harrison and Watson, 1983) meaning that zircon growth is slower than Zr diffusion in the latter case. While we cannot completely rule out a kinetic effect in hydrous magmas, this does not appear a plausible mechanism to explain the observed fractionation in the La Posta pluton.

5.3. Impacts of co-crystallizing phases in other studies

Isotopic effects from titanite may also have influenced zircon isotopic profiles from the Gangdese Batholith (Guo et al., 2020). These profiles are all concave with heavier Zr compositions towards the rims of the grains, an observation consistent, at first-glance, with a primary control of zircon fractionation on $\delta^{94/90}$ Zr in the system. However, and similarly to analyzed grains from the La Posta pluton, there are large variations at both the intragrain (\sim 0.8‰) and intergrain (1.18‰) scales in the Gangdese Batholith samples. These large variations could be caused by, as Méheut et al. (2021) and Tissot and Ibañez-Mejia (2021) proposed, slow diffusion of Zr resulting in a non-uniform distribution of initial Zr isotopic composition throughout the magma. However, the Gangdese batholith, similar to the Peninsular Ranges batholith, is characterized by hydrous magmas (Xu et al., 2015; Ding et al., 2021; Wang et al., 2021; Xia et al., 2021). As discussed earlier, such magmas have higher Zr diffusivities that counteract the pileup effect making slow diffusion an unlikely culprit. Another potential impact for these differences in initial melt compositions is that another phase, like fractionation of amphibole or titanite, are pulling the starting melt composition to isotopically lighter compositions. The zircon isotopic profiles may be further

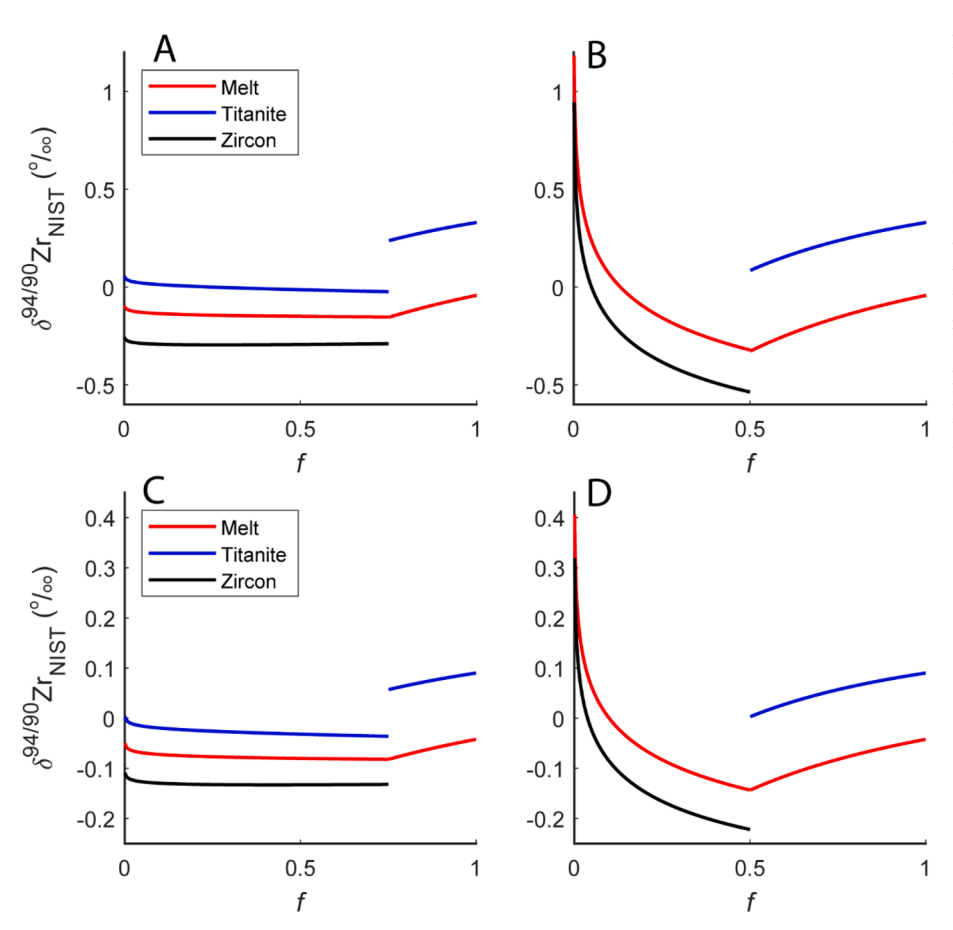


Fig. 14. Fraction of Zr remaining (f) vs. $\delta^{94/90}$ Zr (‰) for a modeled zircon for two systems with 50% of Zr in zircon and 50% of Zr in titanite, both with a constant change in T. Figures A and C show all Zr partitioning into titanite until f = 0.75 followed by cocrystallization of titanite and zircon where 1/3 of Zr partitions into titanite and 2/3 partitions into zircon. In Figures B and D, Zr partitions into titanite until f = 0.5 followed by Zr partitioning into zircon until f = 0. Red, blue, and black lines show the isotopic composition of melt, titanite, and zircon, respectively. Figures A-B show fractionation factors calculated using the ionic model. Figures C-D show profiles calculated using fractionation factors calculated using values from Chen et al. (2020). Please note the different scales between profiles calculated using the ionic model and those calculated using the ab initio method.

impacted by titanite or amphibole fractionation during zircon crystallization which could change the apparent zircon fractionation factor. This would explain why the range of fractionation factors between zircons from each rock is so large. If some zircons are located near a titanite while other zircons are not, the fractionation these two zircons experience will be different and the relationship between temperature and zircon fractionation factor will become harder to constrain.

5.4. Applications to detrital studies and future directions

While Guo et al. (2020) proposed Zr isotopes in zircon as a potential new tool for understanding out-of-context (i.e., detrital) zircons, the caveats discussed here make that goal difficult to achieve at the moment. Ideally, samples from different batholiths would have different ranges in Zr isotopes in zircon. However, as shown in Fig. S3, there are large overlaps in Zr stable isotopes between different batholiths. To use as a potential tool for deciphering out-of-context zircon requires a strong knowledge of magma chemistry and the exact causes of the indicator of interest. Without clear knowledge of co-existing phases, crystallization temperature, and the magma's water content, it does not appear possible to determine the exact causes of observed Zr isotope effects. In principle, assessment of inclusion phases could potentially allow for determination of pre- and co-crystallizing phases, and insights into magma water might be obtained through examination of primary inclusions (Bell et al. 2022; Bell and Kirkpatrick 2022) or trace elements in out-of-context zircons. In practice, however, trace elements have multiple controls including temperature, co-crystallizing phases, and pressure, and will not lead to an unambiguous reconstruction of the exact formation conditions of zircon or the nature of co-crystallizing phases. To understand specifically the impact of co-crystallizing phases on the Zr isotopic composition of zircons, studies of natural sites with known crystallization histories or experimental studies will be needed. Since the two studies that have examined plutonic felsic systems in-depth, this study and that of Guo et al. (2020), are both from areas which formed under hydrous conditions, a potential further path to explore would be to examine insitu samples from an experimental system or samples where R/D>1. This would allow for an in-depth examination of arguments in Méheut et al. (2021) about Zr fractionation being partially controlled by the development of Zr diffusive boundary layers. Another potential method forward to employ other geochemical techniques, such as Hf isotopes, which may provide information about deeper processes in Earth that controls Zr isotope systematics.

6. Summary

In order to gain a greater understanding of Zr isotope behavior in magmatic systems, we performed a suite of Zr isotope analyses in zircon, titanite, amphibole, biotite, and whole rocks from the La Posta pluton, a zoned batholith in the Peninsular Ranges of southern California and undertook simple calculations to assess the role of temperature and cocrystallization effects on producing significant Zr isotopic variations. We found that phases besides zircons, in particular titanite, can significantly impact the Zr isotopic evolution of a system. Yet, these effects, even when incorporating impacts from changing temperature in a system, do not account for the up to 6% variations in zircons seen in the Duluth gabbro or the up to 1.9% variations seen in our La Posta samples. More studies that examine potential controls on Zr isotope evolution will be needed to reach a greater understanding of this nascent isotopic system. Until the responsible processes are better understood, it appears premature to see Zr stable isotopic investigations of igneous rocks as unambiguous proxies for magmatic evolution.

Declaration of Competing Interest

The authors declare that they have no known competing financial interests or personal relationships that could have appeared to influence the work reported in this paper.

Acknowledgement

We thank Mary Reid, Paolo Sossi, and Paul Savage for their helpful reviews which greatly improved this manuscript, Ed Young for help with the ionic model, and Ming-Chang Liu and Andreas Hertwig for assistance with the ion probe. This work was supported by a UCLA Dissertation Year Fellowship and a Geological Society of America student research grant to H.M.K., NSF-EAR 2131632 and 2131643 grants to M.I-M., and by NSF grants EAR-1824002 and MGG-2054892, a Packard Fellowship and Caltech start-up funds to F.L.H.T. The ion microprobe laboratory at UCLA is partially funded by grant EAR-1734856 from NSF's Instrumentation and Facilities program.

Appendix A. Supplementary material

The supplementary material contains one excel spreadsheet with seven sheets and one PDF document. Table S1 contains whole rock major and trace elements, average zircon values, and sample coordinates. Table S2 contains ICPMS-ID analysis of whole rocks and mineral fractions. Table S3 includes U-Pb ages of La Posta zircons. Table 4 contains paired trace element, U-Pb, and Zr analyses names with rock and grain numbers. Table S5 contains Zr stable isotope results for all analyzed La Posta zircon. Table 6 includes zircon trace element analyses, and Table S7 includes Zr stable isotope analysis of geochemical standards. The PDF document includes discussion of the spatial evolution of zircon growth and three supplementary figures. Figure S1 shows grain isotopic profiles calculated using ab initio values from Méheut et al. (2021) and the model proposed in Guo et al. (2020). Figure S2 shows isotopic profiles calculated using different Ti activities, and Figure S3 shows a compilation of Zr isotope ranges of zircons from three batholiths. Supplementary material to this article can be found online at htt ps://doi.org/10.1016/j.gca.2023.05.004.

References

- Akram, W., Schönbächler, M., Sprung, P., Vogel, N., 2013. Zirconium Hafnium isotope evidence from meteorites for the decoupled synthesis of light and heavy neutron-rich nuclei. Astrophys. J. 777.
- Bea, F., Montero, P., Ortega, M., 2006. A LA-ICP-MS evaluation of Zr reservoirs in common crustal rocks: Implications for Zr and Hf geochemistry, and zircon-forming processes. Can. Mineral. 44, 693–714.
- Bell, E.A., Boehnke, P., Harrison, T.M., 2016. Recovering the primary geochemistry of Jack Hills zircons through quantitative estimates of chemical alteration. Geochim. Cosmochim. Acta 191, 187–202.
- Bell, E.A., Boehnke, P., Barboni, M., Harrison, T.M., 2019. Tracking chemical alteration in magmatic zircon using rare earth element abundances. Chem. Geol. 510, 56–71.
- Bell, E.A., Kirkpatrick, H.M., 2021. Effects of crustal assimilation and magma mixing on zircon trace element relationships across the Peninsular Ranges Batholith. Chem. Geol. 586, 120616.
- Bell, E.A., Kirkpatrick, H.M., 2022. Micro-zircon inclusions in accessory minerals reveal more complete magma compositional evolution records. Contrib. Mineral. Petrol. 177, 113.
- Bell, E.A., Kirkpatrick, H.M., Harrison, T.M., 2022. Crystallization order effects on inclusion assemblages in magmatic accessory minerals and implications for the detrital record. Chem. Geo. 613, 121143.
- Bindeman, I.N., Melnik, O.E., 2016. Zircon survival, rebirth and recycling during crustal melting, magma crystallization, and mixing based on numerical modelling. J. Petrol. 57, 437–460.
- Blundy, J., Wood, B., 1994. Prediction of crystal-melt partition coefficients from elastic moduli. Nature 372, 452-454.
- Blundy, J., Wood, B., 2003. Partitioning of trace elements between crystals and melts. Earth Planet. Sci. Lett. 210, 383–397.
- Boehnke, P., Watson, E.B., Trail, D., Harrison, T.M., Schmitt, A.K., 2013. Zircon saturation re-revisited. Chem. Geol. 351, 324–334.
- Chen, X., Wang, W., Zhang, Z., Nie, N.X., Dauphas, N., 2020. Evidence from Ab Initio and transport modeling for diffusion-driven zirconium isotopic fractionation in igneous rocks. ACS Earth Sp. Chem. 4, 1572–1595.

- Clinkenbeard, J.P., Walawender, M.J., 1989. Mineralogy of the La Posta pluton: implications for the origin of zoned plutons in the eastern Peninsular Ranges batholith, southern and Baja California. Am. Mineral. 74, 1258–1269.
- Colombini, L.L., Miller, C.F., Gualda, G.A.R., Wooden, J.L., Miller, J.S., 2011. Sphene and zircon in the Highland Range volcanic sequence (Miocene, southern Nevada, USA): Elemental partitioning, phase relations, and influence on evolution of silicic magma. Mineral. Petrol. 102. 29–50.
- Davidson, J., Turner, S., Handley, H., Macpherson, C., Dosseto, A., 2007. Amphibole "sponge" in arc crust? Geology 35, 787–790.
- Ding, H., Zhang, Z., Kohn, M.J., 2021. Late Cretaceous hydrous melting and reworking of juvenile lower crust of the eastern Gangdese magmatic arc, southern Tibet. Gandwana Res
- Farges, F., Ponader, C.W., Brown, G.E., 1991. Structural environments of incompatible elements in silicate glass/melt systems: I. Zirconium at trace levels. Geochim. Cosmochim. Acta 55. 1563–1574.
- Feng, L., Hu, W., Jiao, Y., Zhou, L., Zhang, W., Hu, Z., Liu, Y., 2020. High-precision stable zirconium isotope ratio measurements by double spike thermal ionization mass spectrometry. J. Anal. At. Spectrom. 35, 736–745.
- Ferry, J.M., Watson, E.B., 2007. New thermodynamic models and revised calibrations for the Ti-in-zircon and Zr-in-rutile thermometers. Contrib Mineral Petrol 154, 429–437.
- Gastil, G., Diamond, J., Knaack, C., Walawender, M., Marshall, M., Boyles, C., Chadwick, B., Erskine, B., 1990. The problem of the magnetite/ilmenite boundary in southern and Baja California. Geol. Soc. Am. Mem. 174, 19–32.
- Gastil, R.G., Phillips, R.P., Allison, E.C., 1975. Reconnaissance Geology of the State of Baja California. In: Gastil, R.G., Phillips, R.P., Allison, E.C. (Eds.), Reconnaissance Geology of the State of Baja California. Geological Society of America.
- Grove, M., Lovera, O., Harrison, T.M., 2003. Late Cretaceous cooling of the east-central Peninsular Ranges batholith (33°N): Relationship to la Posta pluton emplacement, Laramide shallow subduction, and forearc sedimentation. Spec. Pap. Geol. Soc. Am. 374, 355–379.
- Guo, J.-L., Wang, Z., Zhang, W., Moynier, F., Cui, D., Hu, Z., Ducea, M.N., 2020. Significant Zr isotope variations in single zircon grains recording magma evolution history. Proc. Natl. Acad. Sci. 117, 21125–21131.
- Hammarstrom, J.M., Zen, E., 1986. Aluminum in hornblende: an empirical igneous geobarometer. Am. Mineral. 71, 1297–1313.
- Harper, B.E., Miller, C.F., Koteas, G.C., Cates, N.L., Wiebe, R.A., Lazzareschi, D.S., Cribb, J.W., 2004. Granites, dynamic magma chamber processes and pluton construction: The Aztec Wash pluton, Eldorado Mountains, Nevada, USA. Spec. Pap. Geol. Soc. Am. 389, 277–295.
- Harrison, T.M., Watson, E.B., 1983. Kinetics of zircon dissolution and zirconium diffusion in granitic melts of variable water content. Contrib. Mineral. Petrol. 84, 66–72.
- Hayden, L.A., Watson, E.B., 2007. Rutile Saturation in hydrous siliceous melts and its bearing on Ti-thermometry of quartz and zircon. Earth Planet. Sci. Lett. 258 (3–4), 561–568.
- Hayden, L.A., Watson, E.B., Wark, D.A., 2008. A thermobarometer for sphene (titanite). Contrib Mineral Petrol 155, 529–540.
- Hirata, T., 2001. Determinations of Zr isotopic composition and U-Pb ages for terrestrial and extraterrestrial Zr-bearing minerals using laser ablation-inductively coupled plasma mass spectrometry: Implications for Nb-Zr isotopic systematics. Chem. Geol. 176, 323–342.
- Hirata, T., Yamaguchi, T., 1999. Isotopic analysis of zirconium using enhanced sensitivity-laser ablation-multiple collector-inductively coupled plasma mass spectrometry. J. Anal. At. Spectrom. 14, 1455–1459.
- Huang, C., Wang, H., Yu, H.M., Feng, L.P., Xie, L.W., Yang, Y.H., Wu, S.T., Xu, L., Yang, J. H., 2021. Further characterization of SA01 and SA02 zircon reference materials for Si and Zr isotopic compositions: Via femtosecond laser ablation MC-ICP-MS. J. Anal. At. Spectrom. 36, 2192–2201.
- Ibañez-Mejia, M., Tissot, F.L.H., 2019. Extreme Zr stable isotope fractionation during magmatic fractional crystallization. Sci. Adv. 5, 1–14.
- Ibañez-Mejia, M., Tissot, F.L.H., 2021. Reading the Isotopic Code of Heavy Elements. Elements 17, 379–382.
- lizuka, T., Lai, Y.J., Akram, W., Amelin, Y., Schönbächler, M., 2016. The initial abundance and distribution of 92Nb in the Solar System. Earth Planet. Sci. Lett. 439, 172–181.
- Inglis, E.C., Creech, J.B., Deng, Z., Moynier, F., 2018. High-precision zirconium stable isotope measurements of geological reference materials as measured by double-spike MC-ICPMS. Chem. Geol. 493, 544–552.
- Inglis, E.C., Moynier, F., Creech, J., Deng, Z., Day, J.M.D., Teng, F.Z., Bizzarro, M., Jackson, M., Savage, P., 2019. Isotopic fractionation of zirconium during magmatic differentiation and the stable isotope composition of the silicate Earth. Geochim. Cosmochim. Acta 250, 311–323.
- Kimbrough, D.L., Smith, D.P., Mahoney, J.B., Moore, T.E., Grove, M., Gordon, R., Ortegarivera, A., Fanning, C.M., Kimbrough, D.L., Diego, S., 2001. Forearc-basin sedimentary response to rapid Late Cretaceous batholith emplacement in the Peninsular Ranges of southern and Baja California. Geology 29, 491–494.
- Klaver, M., MacLennan, S.A., Ibañez-Mejia, M., Tissot, F.L.H., Vroon, P.Z., Millet, M.A., 2021. Reliability of detrital marine sediments as proxy for continental crust composition: The effects of hydrodynamic sorting on Ti and Zr isotope systematics. Geochim. Cosmochim. Acta 310, 221–239.
- Krummenacher, D., Doupont, J., 1975. K-Ar Apparent Ages, Peninsular Ranges Batholith, Southern California and Baja California. Bull. Geol. Soc. Am. 86, 760–768.
- Liu, M.C., McKeegan, K.D., Harrison, T.M., Jarzebinski, G., Vltava, L., 2018. The Hyperion-II radio-frequency oxygen ion source on the UCLA ims1290 ion microprobe: Beam characterization and applications in geochemistry and cosmochemistry. Int. J. Mass Spectrom. 424, 1–9.

- Louvel, M., Sanchez-Valle, C., Malfait, W.J., Testemale, D., Hazemann, J.L., 2013. Zr complexation in high pressure fluids and silicate melts and implications for the mobilization of HFSE in subduction zones. Geochim. Cosmochim. Acta 104, 281–299
- Mahon, K.I., 1996. The New "York" Regression: Application of an Improved Statistical Method to Geochemistry. Int. Geol. Rev. 38, 293–303.
- Méheut, M., Ibañez-Mejia, M., Tissot, F., 2021. Drivers of zirconium isotope fractionation in Zr-bearing phases and melts: The roles of vibrational, nuclear field shift and diffusive effects. Geochim. Cosmochim. Acta 292, 217–234.
- Miggins, D.P., Premo, W.R., Snee, L.W., Yeoman, R., Naeser, N.D., Naeser, C.W., Morton, D.M., 2014. Thermochronology of Cretaceous batholithic rocks in the northern Peninsular Ranges batholith, southern California: Implications for the Late Cretaceous tectonic evolution of southern California. Mem. Geol. Soc. Am. 211, 199–261
- Minster, J.F., Allègre, C.J., 1982. The isotopic composition of zirconium in terrestrial and extraterrestrial samples: implications for extinct 92Nb. Geochim. Cosmochim. Acta 46, 565–573
- Minster, J.F., Ricard, L.P., 1981. The isotopic contosition of zirconium. Int. J. Mass Spectrom. Ion Phys. 37, 259–272.
- Mungall, J.E., Dingwell, D.B., Chaussidon, M., 1999. Chemical diffusivities of 18 trace elements in granitoid melts. Geochim. Cosmochim. Acta 63, 2599–2610.
- Ortega-Rivera, A., 2003. Geochronological constraints on the tectonic history of the Peninsular Ranges batholith of Alta and Baja California: Tectonic implications for western México. Spec. Pap. Geol. Soc. Am. 374, 297–335.
- Poletti, J.E., Cottle, J.M., Hagen-Peter, G.A., Lackey, J.S., 2016. Petrochronological Constraints on the Origin of the Mountain Pass Ultrapotassic and Carbonatite Intrusive Suite, California. J. Petrol. 57, 1555–1598.
- Premo, W.R., Morton, D.M., Wooden, J.L., Fanning, C.M., 2014. U-Pb zircon geochronology of plutonism in the northern Peninsular Ranges batholith, southern California: Implications for the Late Cretaceous tectonic evolution of southern California. Mem. Geol. Soc. Am. 211, 145–180.
- Quidelleur, X., Grove, M., Lovera, O.M., Harrison, T.M., Yin, A., Ryerson, F.J., 1997.
 Thermal evolution and slip history of the Renbu Zedong Thrust, southeastern Tibet.
 J. Geophys. Res. Solid Earth 102, 2659–2679.
- Reid, M.R., Coath, C.D., Harrison, T.M., McKeegan, K.D., 1997. Prolonged residence times for the youngest rhyolites associated with Long Valley Caldera: 230Th—238U ion microprobe dating of young zircons. Earth Planet. Sci. Lett. 150, 27–39.
- Reid, M.R., Vazquez, J.A., Schmitt, A.K., 2011. Zircon-scale insights into the history of a Supervolcano, Bishop Tuff, Long Valley, California, with implications for the Ti-inzircon geothermometer. Contrib. Mineral Petrol. 161, 293–311.
- Robinson, K., Gibbs, G.V., Ribbe, P.H., 1971. The Structure of Zircon: a Comparison With Garnet. Am. Mineral. 56, 782–790.
- Schmitt, A.K., 2011. Uranium Series Accessory Crystal Dating of Magmatic Processes. Annu. Rev. Earth Planet. Sci. 39, 321–349.
- Schmitz, M.D., Bowring, S.A., Ireland, T.R., 2003. Evaluation of Duluth Complex anorthositic series (AS3) zircon as a U-Pb geochronological standard: New highprecision isotope dilution thermal ionization mass spectrometry results. Geochim. Cosmochim. Acta 67, 3665–3672.
- Schönbächler, M., Lee, D.C., Rehkämper, M., Halliday, A.N., Fehr, M.A., Hattendorf, B., Günther, D., 2003. Zirconium isotope evidence for incomplete admixing of r-process components in the solar nebula. Earth Planet. Sci. Lett. 216. 467-481.
- Schönbächler, M., Rehkämper, M., Fehr, M.A., Halliday, A.N., Hattendorf, B., Günther, D., 2005. Nucleosynthetic zirconium isotope anomalies in acid leachates of carbonaceous chondrites. Geochim. Cosmochim. Acta 69, 5113–5122.
- Shaw, S.E., Todd, V.R., Grove, M., 2003. Jurassic peraluminous gneissic granites in the axial zone of the Peninsular Ranges, southern California. Spec. Pap. Geol. Soc. Am. 374, 157–183.
- Shaw, S.E., Todd, V.R., Kimbrough, D.L., Pearson, N.J., 2014. A west-to-east geologic transect across the Peninsular Ranges batholith, San Diego County, California: Zircon 176Hf/177Hf evidence for the mixing of crustal- and mantle-derived magmas, and comparisons with the Sierra Nevada batholith. Mem. Geol. Soc. Am. 211, 499–536.
- Silver, L.T., Chappell, B.W., 1988. The Peninsular Ranges Batholith: An insight into the evolution of the Cordilleran batholiths of southwestern North America. Trans. R. Soc. Edinb. Earth Sci. 79, 105–121.
- Silver, L.T., Taylor Jr., H.P., Chappell, B.W., 1979. Some petrological, geochemical, and geochronological observations of the Peninsular Ranges batholith near the International border of the U.S.A. and Mexico. In: Abbot, P.L., Todd, V.R. (Eds.), Mesozoic Crystalline Rocks, Geological Society of America Annual Meeting Guidebook, pp. 83–110.

- Simmons, E.C., Hedge, C.E., 1978. Minor-element and Sr-isotope geochemistry of tertiary stocks, Colorado mineral belt. Contrib. Mineral. Petrol. 67, 379–396.
- Speer, J.A., Gibbs, G.V., 1976. The crystal structure of synthetic titanite, CaTiOSiO4, and the domain textures of natural titanites. Am. Mineral. 61, 238–247.
- Tian, S., Inglis, E.C., Creech, J.B., Zhang, W., Wang, Z., Hu, Z., Liu, Y., Moynier, F., 2020. The zirconium stable isotope compositions of 22 geological reference materials, 4 zircons and 3 standard solutions. Chem. Geol. 555, 119791.
- Tissot, F., Ibañez-Mejia, M., 2021. Unlocking the Single-Crystal Record of Heavy Stable Isotopes. Elements 17, 389–394.
- Todd, V.R., Shaw, S.E., 1985. S-type granitoids and an I-S line in the Peninsular Ranges batholith, southern California. Geology 13, 231–233.
- Tompkins, H.G.D., Zieman, L.J., Ibañez-Mejia, M., Tissot, F.L.H., 2020. Zirconium stable isotope analysis of zircon by MC-ICP-MS: methods and application to evaluating intra-crystalline zonation in a zircon megacryst. J. Anal. At. Spectrom. 35, 1167–1186
- Tompkins, H.G.D., Ibañez-Mejia, M., Tissot, F.L.H., Bloch, E., Wang, Y., Trail, D., 2023. Zircon growth experiments reveal limited equilibrium Zr isotope fractionation in magmas. Geochem. Perspect. Lett. 25, 25–29.
- Trail, D., Watson, E.B., Tailby, N.D., 2011. The oxidation state of Hadean magmas and implications for early Earth's atmosphere. Nature 480, 79–82.
- Walawender, M.J., Gastil, G., Clinkenbeard, J.P., Mccormick, W.V., Eastman, B.G., Wernicke, R.S., Wardlaw, M.S., Gunn, S.H., Smith, B.M., 1990. Orgin and evolution of the zoned La Posta-type plutons, eastern Peninsular Ranges batholith, southern and Baja California. Geol. Soc. Am. Mem. 174, 1–18.
- Wang, R.Q., Qiu, J.S., Wen, D.J., Xu, H., 2021. The role of hydrous mantle-derived magmas in the generation of Late Cretaceous granitoids in the Gangdese batholith: insights from the Shanba and Zongga plutons in the southern Lhasa subterrane. Tibet. Mineral. Petrol. 115, 113–136.
- Watson, E.B., 1996. Dissolution, growth and survival of zircons during crustal fusion: kinetic principles, geological models and implications for isotopic inheritance. In: Brown, M., Candela, P.A., Peck, D.L., Stephens, W.E., Walker, R.J., Zen, E. (Eds.), The Third Hutton Symposium on the Origin of Granites and Related Rocks. Geological Society of America, pp. 43–56.
- Watson, E.B., Harrison, T.M., 1983. Zircon saturation revisited: temperature and composition effects in a variety of crustal magma types. Earth Planet. Sci. Lett. 64, 295–304.
- Watson, E.B., Harrison, T.M., 2005. Zircon thermometer reveals minimum melting conditions on earliest Earth. Science. 308, 841–844.
- Whitehouse, M.J., Platt, J.P., 2003. Dating high-grade metamorphism Constraints from rare-earth elements in zircon and garnet. Contrib. Mineral. Petrol. 145, 61–74.
- Wu, T., Zhang, W., Wilde, S.A., 2020. The origin of mafic microgranular enclaves in granitoids: Insights from in situ Sr isotope of plagioclases and Zr-Hf isotopes of zircons. Chem. Geol. 551, 119776.
- Xia, X.P., Meng, J., Ma, L., Spencer, C.J., Cui, Z., Zhang, W.F., Yang, Q., Zhang, L., 2021. Tracing magma water evolution by H₂O-in-zircon: A case study in the Gangdese batholith in Tibet. Lithos 404–405, 106445.
- Xu, W.C., Zhang, H.F., Luo, B., Guo, L., Yang, H., 2015. Adakite-like geochemical signature produced by amphibole-dominated fractionation of arc magmas: An example from the Late Cretaceous magmatism in Gangdese belt, south Tibet. Lithos 232, 197–210.
- Young, E.D., Manning, C.E., Schauble, E.A., Shahar, A., Macris, C.A., Lazar, C., Jordan, M., 2015. High-temperature equilibrium isotope fractionation of nontraditional stable isotopes: Experiments, theory, and applications. Chem. Geol. 395, 176–195.
- Yuan, Y., Guo, J.-L., Zong, K., Feng, L., Wang, Z., Moynier, F., Zhang, W., Hu, Z., Xu, H., 2022. Stable zirconium isotopic fractionation during alkaline magma differentiation: Implications for the differentiation of continental crust. Geochim. Cosmochim. Acta 326. 41–55.
- Zen, E.A., 1986. Aluminum enrichment in silicate melts by fractional crystallization: Some mineralogic and petrographic constraints. J. Petrol. 27, 1095–1117.
- Zhang, W., Wang, Z., Moynier, F., Inglis, E., Tian, S., Li, M., Liu, Y., Hu, Z., 2019. Determination of Zr isotopic ratios in zircons using laser-ablation multiple-collector inductively coupled-plasma mass-spectrometry. J. Anal. At. Spectrom. 34, 1800–1809
- Zhu, Z., Zhang, W., Wang, J., Wang, Z., Guo, J.-L., Hoffman, J.E., Feng, L., Luo, T., Hu, Z., Liu, Y., Moynier, F., 2023. Zr isotope variations in a large granite batholith. Geochim. Cosmochim. Acta. 342, 15–30.